Indian Institute of Science Education and Research, Pune

Faculty & Department of Physics

December, 2024

Properties of gas in and around galaxies at $z < 0.6$ using MALS

Shashank Soni

A Thesis Submitted in Partial Fulfillment
of the Requirements for the

BS-MS Dual Degree Programme

in the Field of Physics

Supervisor: Neeraj Gupta

Certificate

This is to certify that this dissertation entitled *Properties of gas in and around galaxies at* $z < 0.6$ *using MALS*, towards the partial fulfilment of the BS-MS dual degree programme at the Indian Institute of Science Education and Research, Pune, represents the study/work carried out by *Shashank Soni* under the supervision of *Neeraj Gupta*, Professor, Inter-University Centre for Astronomy and Astrophysics, Pune.

Neeraj Gupta

Committee:
Dr. Neeraj Gupta
Dr. Prasad Subramanian

This thesis is dedicated to the idea of IISER Pune.

Declaration

I hereby declare that the matter embodied in the report entitled *Properties of gas in and around galaxies at* $z < 0.6$ *using MALS* are the results of the work carried out by me at The Faculty & Department of Physics, Indian Institute of Science Education and Research, Pune, under the supervision of Neeraj Gupta, and the same has not been submitted elsewhere for any other degree.

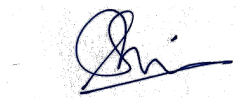

Shashank Soni

Acknowledgements

This thesis represents the culmination of five and a half incredible years at IISER. I've been through some of the highest highs and the lowest lows in my recent memory while being associated with this institute. The people I've met and the moments we've shared have made this journey unforgettable. IISER Pune is not the academics here, the science you study, or the research you do—it was never supposed to be. It's the people, the environment, and the culture that you foster and invite here. That's the abstract idea of IISER that I had in mind, but when I first arrived, it wasn't exactly what I expected. It was an experience, nonetheless. Then COVID messed things even further. Now, I feel that it's straying away from that philosophy even more as time goes by. I hope that IISER gets it's life back in the future.

First and foremost, I would like to express my deepest gratitude to my supervisor, Dr. Neeraj Gupta. His guidance and vision were the foundation of this project, and without his insightful ideas, none of this would have been possible. Every meeting was an opportunity to learn something new, and through his quiet yet steady mentorship, I grew as an academic. He provided me the space to evolve, both intellectually and personally. This journey had its ups and downs—there were times when burnout made it challenging to work, and times when results and calculations flowed effortlessly. Through this thesis, I came to understand what it means to do research.

I also extend my gratitude to all the authors whose work has been referenced in this thesis. Additionally, I am grateful to IISER Pune and IUCAA for providing me with the facilities and resources needed to complete this work.

I want to thank the wider IISER Pune community, particularly the residents of Hostel 1, for being a part of a collective support system. I especially want to thank the friends I made from the hostel balcony, we fondly called Saade 8. It truly turned into a joint family, and I will cherish the memories we made forever. I'm grateful to all the friends I made in my first year who stood by me virtually through the events of the COVID pandemic. I want to thank all the friends I made with my football team, Black Dogs FC. We won the lot you guys. I am also thankful to the gym for providing me with the facilities to establish a routine that helped me push through tough times.

It is said that you find the most beautiful people in the most unexpected walks of your life. A special mention goes to my roommate, Varun, and my close friends, Vachan, Somen and Raghav. You were the people I resonated with the most, and you've been instrumental in my growth over these years.

It is also said that everything in life has an appropriate space and an appropriate time. The fifth-year room at the physics department deserves its own shout-out for that. Without a designated workspace like that, much of this thesis would not have been possible. I also want to acknowledge my room (H1-930), a gathering place open to everyone and a safe haven for me when I needed solace. It was the first personal space I built for myself.

I am also grateful to the student body for organising cultural events that made for a great place to come together. Also a heartfelt thanks to the city of Pune itself, one of the best places to experience student life, especially being at a campus like IISER Pune.

I want to thank my family. They don't always understand me, but they support me unconditionally. They were the bedrock I fell back to when I couldn't find support elsewhere. I'm deeply grateful for their understanding and for giving me the freedom to pursue whatever I wanted in my studies, even though a career in pure science isn't the most colloquial path in the world today.

I also want to acknowledge the privilege that has allowed me to reach where I am. I recognize that many people have worked harder and aspired as much as I have to reach this stage, yet were unable to get here due to an uneven playing field. I commend everyone who continues the fight against class disparities and ignorance, and strives to make this a more equitable and empathetic place.

Finally, I want to thank you, the reader, for being interested in my work.

For this thesis, I stayed up all night, looking at stars.

Slowly, but Surely, everyday Sincerely.

Abstract

This thesis presents a comprehensive study of HI absorption within the interstellar medium of galaxies, focusing on the detection and analysis of absorption signatures using radio spectral data. Initially, we sought to identify absorption features by examining likely candidates, such as galaxy mergers, which could cause flux absorption in the spectra of background sources. Subsequently, through a "blind search" approach, we aimed to detect HI absorption without prior selection of galaxies or objects of interest, enabling the discovery of cold gas systems along the line of sight. This unbiased method offers fresh insights into the interactions between galaxies and their surrounding environments.

First, our investigation leveraged data from two major sources: the Galaxy Zoo DESI (GZD) catalog and the MeerKAT Absorption Line Survey (MALS). Using a machine learning model from the literature trained on Galaxy Zoo morphology classifications, we identified 109 potential galaxy mergers, narrowing this down to 38 galaxy-source pairs based on specific criteria, such as proximity to strong radio sources and peak flux densities of those sources. The primary objective was to examine these pairs for HI absorption signatures by analyzing the overlap between radio contours and optical images.

We performed spectral analysis on the most promising radio sources, applying a boxcar smoothing technique to enhance the detection of absorption lines. Despite an extensive search, no significant HI absorption was detected in our initial sample. We calculated upper limits on optical depth and column density for non-detections, which provide valuable constraints on the neutral gas content of these systems.

In addition, we present a detailed case study of the galaxy NGC5363, which was identified through a blind search of spectra. The spectral data, processed similarly after the ARTIP pipeline, exhibited notable signs of HI absorption, highlighting the potential of this technique to reveal cold gas systems in galaxies.

This thesis contributes to the field by demonstrating the effectiveness of blind spectral searches for detecting cold gas and offers new insights into the ISM of galaxy mergers. Our findings contribute to ongoing studies aimed at probing the connection between galaxy interactions, ISM content, and star formation activity across cosmic time.

Contents

List of Figures

List of Tables

CHAPTER 1

INTRODUCTION

1.1. Galaxies

In astrophysics, galaxies represent the fundamental building blocks of the large-scale structure of the universe. These massive systems consist of stars, gas, dust, dark matter, and other cosmic elements. Galaxies are not solitary entities; they are embedded in groups, clusters, and superclusters, interconnected by dark matter filaments and bound together by gravity. This intricate network allows galaxies to trace the large-scale structure of the universe, offering insights into how matter is distributed and how it has evolved since the early universe.

Galaxies are dynamic environments where star formation is continuously occurring. Gas clouds within galaxies collapse under gravity to give birth to stars, and this process is shaped by galactic dynamics, feedback from supernovae, and interactions with neighboring galaxies. Galaxies primarily grow through mergers, where the collision and combination of galaxies trigger bursts of star formation and alter their structure, changing both their shape and size.

Moreover, galaxies serve as laboratories for investigating both local and global cosmic phenomena. On a smaller scale, they allow the study of star formation, the evolution of active galactic nuclei (AGN), and the chemical composition of the universe. On a larger scale, they provide insights into the large-scale structure of the universe, the nature of dark matter and dark energy, and the processes driving cosmic evolution.

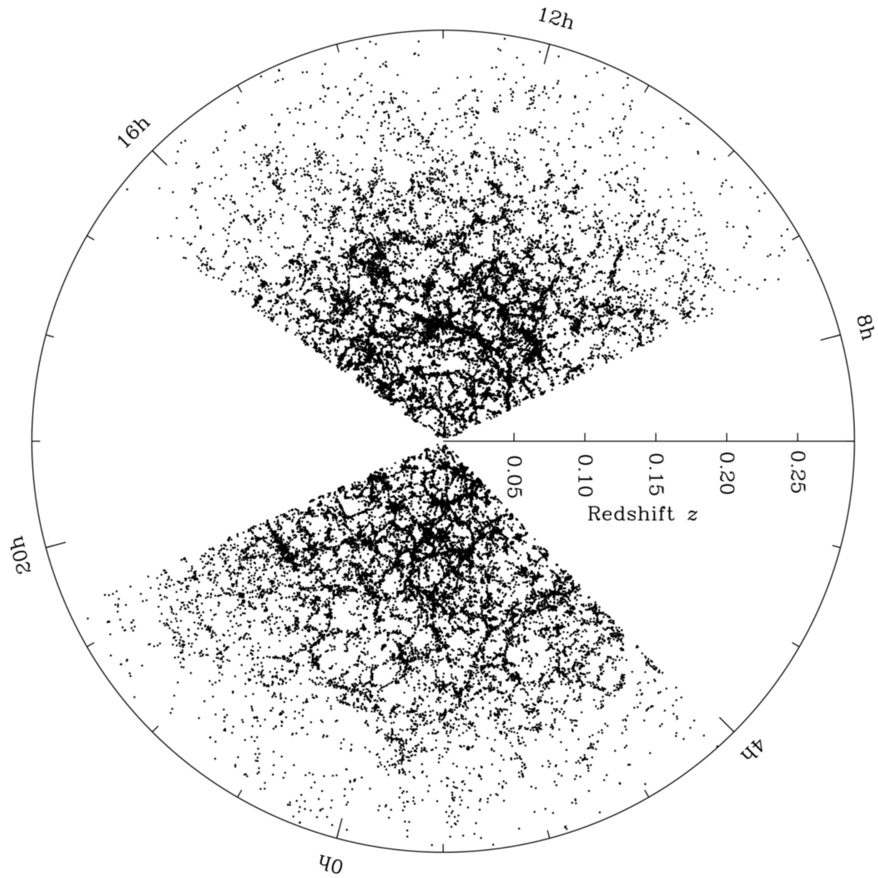

Figure 1.1.: Spatial distribution of galaxies as a function of redshift and right ascension [1]

1.2. The Interstellar Medium

The interstellar medium, or ISM, is the gas and dust that permeate the space between stars inside the galaxy. The ISM plays a critical role in the formation of stars, which are the primary sources of energy within a galaxy. Most of the energy emitted by galaxies is derived from nuclear fusion in stars and the gravitational energy released in accretion disks surrounding black holes. [2]

In the early stages of galactic evolution, the ISM primarily consisted of baryonic matter. As galaxies evolve, the ISM is gradually converted into stellar nurseries, where stars form. However, some of the gas in the ISM is ejected via the galactic winds or stripped off by the intergalactic medium. Additionally, gas infall from the intergalactic medium can increase the ISM's mass. In the present-day Milky Way, most baryons are locked within stars or stellar remnants, with approximately 10% of the baryons residing in the ISM. [2]

These baryons in the ISM exist across a wide range of temperatures and densities. The dynamic nature of the ISM allows for all densities and temperatures within these ranges to coexist in the Milky Way. Despite this variability, most baryons tend to congregate in distinct 'phases'. The ISM consists of various phases such as the Hot Ionized Medium

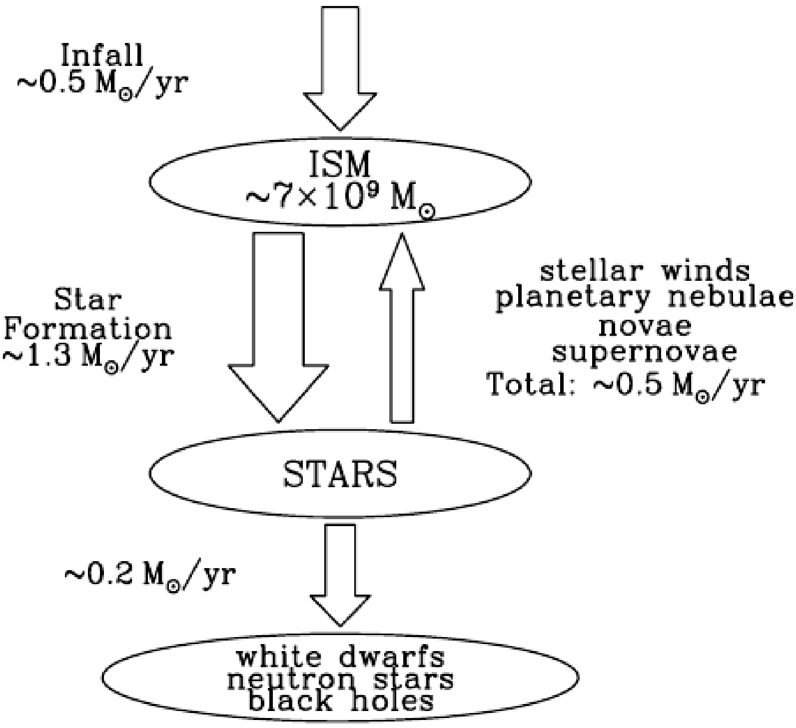

Figure 1.2.: Baryon Flow in Milky Way [2]

(HIM), HII regions, Warm Neutral Medium (WNM), Cold Neutral Medium (CNM), diffuse molecular gas, dense molecular gas, and stellar outflows. These are listed in detail in Appendix A (Figure A.1). [2]

Among these phases, star formation occurs within the cold neutral and molecular regions. The examination of cold molecular gas within the ISM is crucial, as it directly correlates with the efficiency of gas conversion into molecular gas, and subsequently, star formation. The Cold Neutral Medium (CNM), typically found at temperatures around 100 K, is the region within the ISM where star formation primarily takes place. Unlike hot gases, which lacks the ability to clump together, the CNM is capable of coalescing under external disturbances, thereby triggering radiation emission and the collapse of gas clouds within stellar nurseries, and leading to the birth of new stars.

The presence of neutral atomic hydrogen (HI) within the CNM is a critical indicator of an environment conducive to star formation. HI is shielded from ionizing radiation, allowing it to serve as a precursor to molecular hydrogen clouds, which are also essential for the formation of stars. Alongside HI, other molecular species coexist within these cold regions, contributing to the complex gas dynamics that drive star formation in galaxies.

Thus, observing HI within the CNM provides invaluable insights into the cold gas content of galaxies, the star formation rates (SFR) at different epochs, and also the overall mass content and kinematics of galaxies.[2]

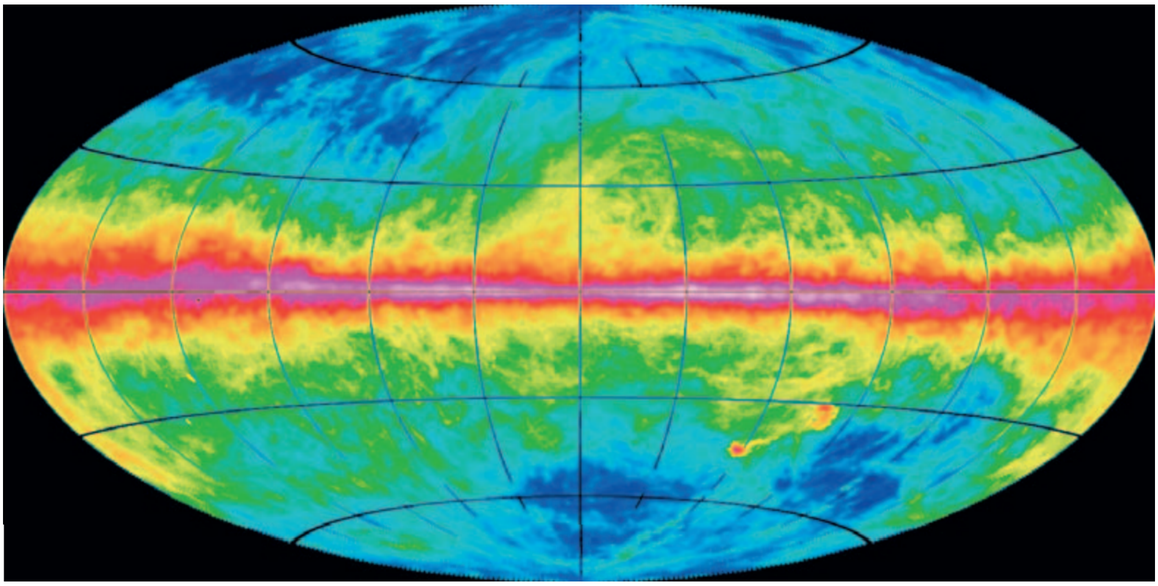

Figure 1.3.: HI emission in Milky Way integrated over the velocity range of 800 km/s [3]

1.3. HI 21-cm as a Tracer of Atomic Gas

Hydrogen is the most abundant element in the universe, and galaxies are primarily composed of it. As the main fuel for star formation, hydrogen contributes significantly to the dynamics and evolution of galaxies. It exists in several states, including molecular hydrogen (H_2), neutral atomic hydrogen (HI), and ionized hydrogen (HII), with HI being the most prevalent phase. Approximately 60% of hydrogen exists as neutral atomic hydrogen, 20% as molecular hydrogen, and 20% in the ionized state.

HI, or neutral atomic hydrogen, plays a critical role in astrophysical studies due to its usefulness as a tracer of cold gas. One of the key ways we observe HI is through the 21-cm radio emission line, which results from the hyperfine transition in the electron's spin state within the hydrogen atom (Figure 1.4). This 21-cm line enables astronomers to study the distribution, temperature, density, kinematics, and chemical composition of HI gas. The HI 21-cm line is especially useful for tracing the cold neutral medium (CNM) within galaxies, offering insight into both galactic and cosmological processes.[2]

The splitting energy between the two spin states is small, $E_u - E_l = 5.87 \times 10^{-6} eV$, therefore the upper spin states are essentially populated by self-collisions or the ambient cosmic microwave background itself. When the electron drops to the ground state, the electron spin flips, and a photon is emitted with a wavelength $\lambda = 21.11$ cm.

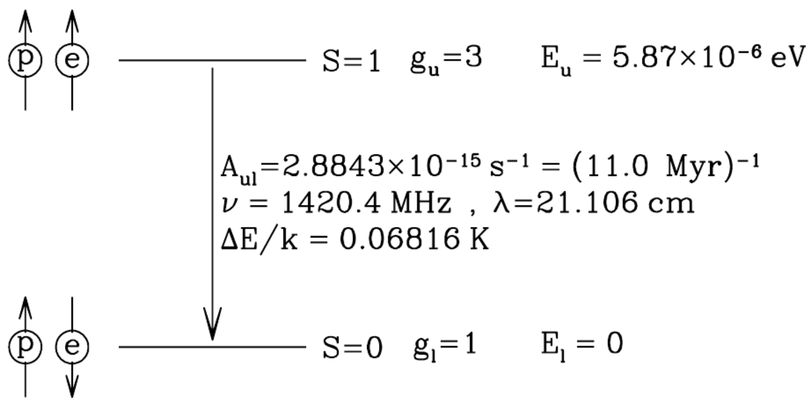

Figure 1.4.: Hyperfine Splitting of HI [2]

For the excitation temperature (T_x), the fraction of atoms in upper and lower energy states is given by;

$$\frac{n_U}{n_L} = \frac{g_U}{g_L} exp\Big(-\frac{h\nu_o}{kT_x}\Big) \tag{1.1}$$

where the degeneracy for the upper spin state of an HI atom $g_U = 3$ and for the lower spin state $g_L = 1$. This gives us, $n_U \approx \frac{3}{4}n(HI)$. [4]

Analogous to the excitation temperature (or state temperature), we can also define the spin temperature (T_s) of HI atom in the context of HI 21-cm line. The spin temperature essentially represents the balance between radiative and collisional processes in the gas. In thermal equilibrium, the spin temperature is influenced by the spontaneous emission rate and the collision rate. If spontaneous emission dominates, the spin temperature tends toward the brightness temperature of the gas. If collisions dominate, the spin temperature approximates the kinetic temperature of the gas. In local thermal equilibrium (LTE), all three temperatures—spin, brightness, and kinetic—converge at a singular value. Also at LTE, the number of transitions is proportional to the Boltzmann factor $e^{-\Delta E/kT_s}$, where ΔE is the difference in energy between the two spin states. Regardless of whether the HI is in LTE or not, we can always define the HI spin temperature. The spin temperature provides crucial information about the fractions of HI gas in the cold and warm phases. It is the harmonic mean of the temperatures of the cold neutral medium (CNM) and the warm neutral medium (WNM). [9]

1.3.1. Radiative Transfer

During the propagation of a radio wave, it can pass through a host of intervening medium, like interstellar clouds or the Earth's atmosphere, which can both absorb incoming wave energy, and also emit its own energy. [5]

To take this into account, we define the quantities, specific emissivity j_ν and linear absorption coefficient κ_ν. The former is the power emitted per unit volume, per frequency interval, per steradian, or equivalently the specific intensity added per unit distance through the medium, $j_\nu = (dE/dt)/\Omega d\nu dV$. And the latter is the fraction of incident power lost while the radiation passes through unit distance, $\kappa_\nu = -dI_\nu/I_\nu ds$. The integral of κ_ν with the linear length is defined as, optical length;

$$\tau_\nu = \int_0^s \kappa_\nu(s')ds' \tag{1.2}$$

If κ_ν is large then it implies strong attenuation, and the medium is termed as optically thick; in the limit $\kappa_\nu \to \infty$ it is completely opaque and we only observe a surface layer. If κ_ν is small then the medium is termed optically thin and in the limit $\kappa_\nu \to 0$ it is completely transparent. The case where $\kappa_\nu = 1$ marks the transition between the optically thin and optically thick regimes. [5]

Using the equilibrium condition, where the change in specific intensity (dI_ν) is proportional to the specific intensity (I_ν), we can write the equation of radiative transfer for the system;

$$\frac{dI_\nu}{ds} = j_\nu - \kappa_\nu I_\nu \tag{1.3}$$

Considering the quantum effects, the linear absorption coefficient can also be written as;

$$\kappa(\nu) = \frac{3c^2}{32\pi}\frac{h}{kT_s}\frac{A_{UL}n(HI)}{\nu_o}\phi(\nu) \tag{1.4}$$

where A_{UL} is the einstein coefficient for spontaneous emission rate for the two spin states, $n(HI)$ is the number of neutral hydrogen atoms per cm^3, ν_o is frequency of photon emitted by this transition, and $\phi(\nu)$ is the HI line profile which is usually considered to be a gaussian. [4]

1.3.2. Observables of 21-cm line

Since $\int n(HI)ds = N(HI)$, and τ is the line integral of κ (equation 1.2), we can integrate the equation (1.4) over the line of sight, considering the spin temperature to be constant. Inverting the equation (1.4) to the side of column density we find that:

$$\frac{dN(HI)}{d\nu} = \frac{32\pi}{3\lambda_o^2}\frac{k}{hcA_{ul}}T_{\text{spin}}(\nu)\tau(\nu) \tag{1.5}$$

where ν_o has been converted to λ_o. Thus the HI column density per unit velocity can be derived from absorption observations if we assume the value of spin temperature. This can be simplified to by putting in the values of constants:

$$\frac{dN(HI)}{d\nu} = 1.823 \times 10^{18}\frac{T_{\text{spin}}(\nu)}{K}\frac{\tau(\nu)}{\text{km/s}}. \tag{1.6}$$

For the optically thin limit (ie, $\tau << 1$), where self-absorption can be neglected, observation of the 21-cm emission line of HI provides direct measurements of the total HI column density. [2] At this limit, $T_s\tau(\nu) \approx T_b$, the brightness temperature of the HI emission line, which can be substituted in equation 1.6 and column density, $N(\text{HI})$, can be calculated using the following equation:

$$\frac{dN(HI)}{dv} = 1.823 \times 10^{18}\frac{T_b(v)}{K} \tag{1.7}$$

where $T_b(v)$ is the brightness temperature of the HI emission line as a function of velocity, v. [4] The brightness of an optically thin radio emission line is proportional to the column density of emitting gas but can be nearly independent of the gas temperature.

Similarly for the optically thin regime, total HI mass in the gas can also be determined from the observed flux of 21-cm line (F_ν);

$$\frac{M_{HI}}{M_\odot} = 2.343 \times 10^5(1+z)\Big(\frac{D_L}{Mpc}\Big)^2\Big(\frac{\int F_\nu d\nu}{Jykms^{-1}}\Big) \tag{1.8}$$

HI 21-cm emission provides a direct measure of the total column density of neutral hydrogen. Meanwhile, HI 21-cm absorption measures the optical depth, and by assuming the spin temperature of medium, we can get column density of neutral hydrogen by absorption. By combining both emission and absorption data, one can estimate the spin temperature of the medium from equation 1.5. In optically thin regions, where only emission occurs, we can set upper bounds on both the optical depth (τ) and spin temperature (T_{spin}). However, in optically thick regions, where both emission and absorption occur, we can determine the precise values of both τ and T_{spin}. [2]

1.3.3. HI Emission and Absorption

The detection and study of atomic hydrogen rely on its 21-cm emission and absorption lines. HI 21-cm emission observations are limited by resolution effects and the detection limit of column density, especially at higher redshifts where the line becomes fainter. At such distances, HI is often detected through 21-cm absorption when it lies between the observer and a strong background radio source. The complementary nature of HI 21-cm emission and absorption observations allows astronomers to study the gas across different redshift ranges: emission is more effective at lower redshifts, while absorption is more sensitive at higher redshifts. [10][11]

The study of HI absorption is particularly sensitive to the cold phase of the ISM. The CNM, characterized by its low temperature, absorbs more strongly than the WNM, making HI absorption an excellent tool for probing the cold gas content of galaxies. [4]

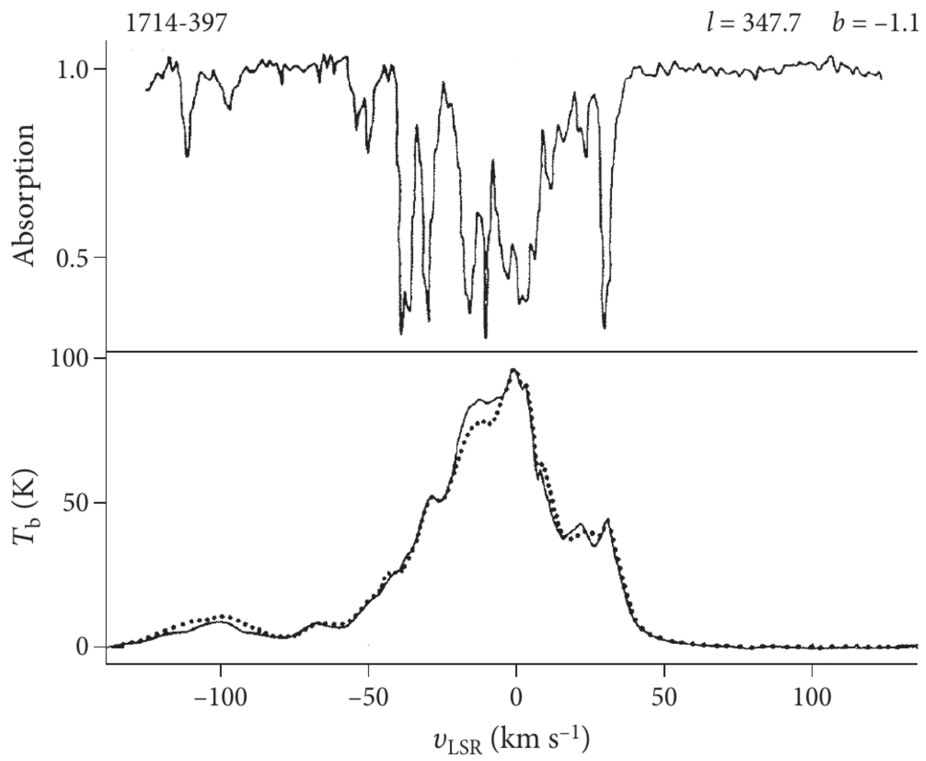

Figure 1.5.: HI absorption and emission spectra toward a source 1714-397 [4]

1.3.4. Intervening & Associated 21-cm Absorption

There are essentially two type of HI absorption systems that we can observe outside the Milky Way. When a gas cloud lies in the line of sight to a background radio source, some amount of flux is absorbed by the intervening gases. The redshift of the absorption feature differs from the redshift of the background source in this case. This phenomenon is referred to as intervening absorption. For this, only a fraction of the gas is observed, usually representing an incomplete view of the intervening gas.

In contrast, associated absorption occurs when the absorption takes place in the immediate vicinity of the radio source itself. This can happen in cases where the absorbing gas is infalling, dust-obscured, or part of the host galaxy itself of an active galactic nucleus (AGN). For associated absorption systems, the absorption signature appears at the redshift of the background source, providing insights into the local conditions around the AGN or other cosmic objects. Observed parameter in this case are local to the galaxy.

1.3.5. HI Line Profile

Extragalactic signatures of HI emission and absorption typically display distinctive line profiles, often characterized as either a singular peak or a double-horned shape. These profiles arise due to the dynamics of the gas in galaxies and are commonly modeled using Gaussian or Voigt profiles. The double-horned profiles, which are indicative of rotating gas within a galaxy, are usually modeled through multi-component Gaussian functions or sometimes using a "busy function" [12] to capture the complexity of the emission.

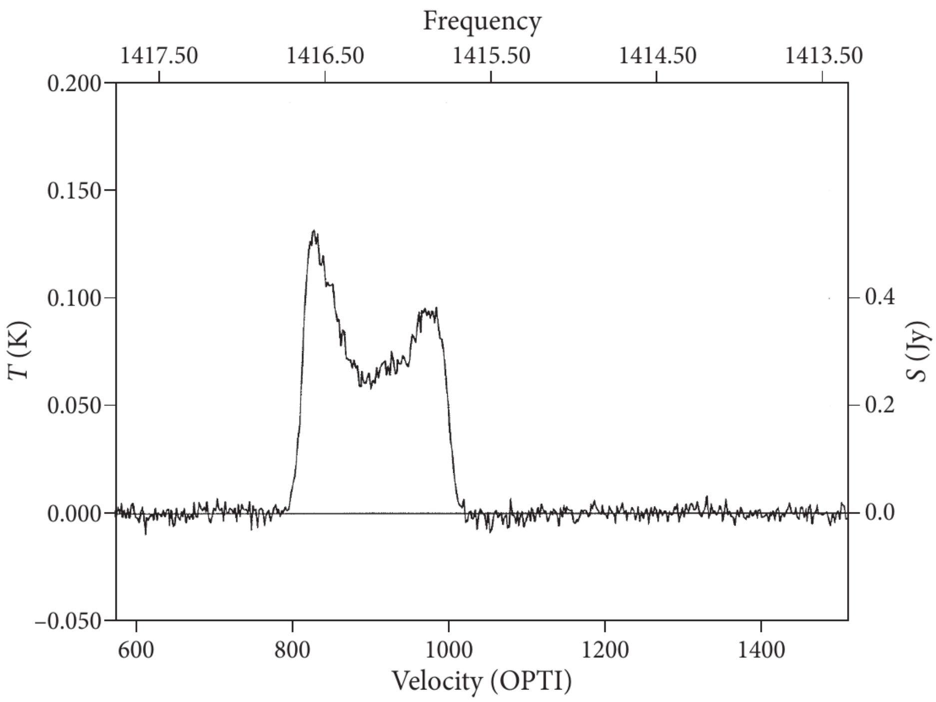

Figure 1.6.: The double-horned HI profile for a spiral galaxy [4]

In addition to the profile shape, the line width provides valuable information about the gas. Broader lines can indicate higher gas temperatures or increased internal microscopic motion (Doppler broadening). The position of the emission or absorption line in frequency (or velocity) space is redshifted due to the cosmological expansion of the universe. Additionally, this signature can be further shifted because of the bulk radial velocity of the gas or galaxy, a phenomenon known as Doppler shift. [5]

The area under the emission profile is a key indicator of the mass of the gas cloud, while the area under the absorption profile provides information on the integrated optical depth of the cloud. Both emission and absorption profiles can be used to infer the HI column density, which provides a measure of the amount of neutral hydrogen gas along the line of sight.

1.4. Star Formation Rate

Studying the star formation rate (SFR) of the universe across different epochs is crucial for understanding the evolutionary history of galaxies over cosmic time. By assessing the SFR at various epochs, astronomers gain insights into how star formation rates have evolved from the early universe to the present day. Essentially, the SFR acts as a cosmic chronometer, enabling astronomers to establish timelines for the formation and development of galaxies. Deep galaxy surveys have revealed that the global star formation rate density peaks within the redshift range of $1 \leq z \leq 2$, followed by a sharp decline towards $z = 0$. However, the underlying mechanisms, particularly the evolution of the cold atomic ($\sim 100\,\mathrm{K}$) and molecular gas phases driving this evolution, remain not fully understood. [13]

External interactions, such as merger events (collisions or tidal interactions), can significantly impact the SFR of galaxies by disturbing their gas reservoirs through processes like gas compression and shock waves. Studying cold gas in merger events offers valuable insights into the SFR density across different cosmic epochs.

1.5. Outline

The objective of this project is to develop a comprehensive understanding of the general characteristics of intervening HI absorbers in the vicinity of nearby galaxies, particularly within the redshift range $0 \leq z \leq 0.6$. By analyzing absorption lines detected in the spectra of radio sources, we can correlate these properties with those of galaxies emitting HI 21-cm emission observed in surveys like MALS. This approach facilitates the interpretation of high-redshift HI absorption, where galaxies may be challenging to detect due to their proximity to bright quasars in optical/UV wavelengths. Additionally, at $z > 0.05$, the

HI 21-cm signal becomes faint, making absorption studies more viable for tracing cold gas. Ultimately, such studies provide insights into the distribution of cold gas within and around galaxies and its correlation with the SFR. [14]

Subsequently, we will utilize multi-wavelength data from surveys like MALS and DESI to construct a sample of galaxies suitable for achieving the project's objectives. Finally, this sample will undergo detailed analysis to characterize both the HI 21-cm absorption lines and the galaxies themselves. The analysis aims to understand the distribution of cold gas in and around galaxies, interpret high-redshift HI absorption, and correlate these findings with the SFR of galaxies.

Chapter 1 has provided an introduction to the overarching concept for this project. This chapter has also provided an overview of the star formation rate (SFR) across cosmic time, its significance, and the key role played by cold gas in galaxy evolution. It will also introduce the objectives of the study and the motivation for focusing on HI absorption in the redshift range $0 \leq z \leq 0.6$.

Chapter 3 will describe the MeerKAT Absorption Line Survey (MALS) and the methodology for extracting HI absorption data from the MALS.

Chapter 4 will explore how external interactions, particularly galaxy mergers, impact the distribution of cold gas and the SFR of galaxies. It will delve into case studies and examples of mergers where significant absorption by HI was expected to have been observed.

Chapter 5 will focus on the blind search methodology used to identify intervening HI absorbers. It will also detail a case study were HI absorption was observed, and quantities like optical depth and HI column densities were calculated which agreed with the values published in different literature.

Chapter 6, the final chapter, will summarize the key findings of the project and their implications for the study of galaxy evolution. It will also suggest directions for future research in this area.

CHAPTER 2

METHODOLOGY

2.1. Radio Interferometry

Radio waves possess the unique ability to penetrate through dust and gas due to their longer wavelengths, a characteristic not shared by most other forms of electromagnetic radiation. This property is particularly advantageous in astronomical observations, as Earth's atmosphere is largely transparent to a significant portion of the radio spectrum, specifically in the centimeter to meter range. As a result, large radio observatories can be built on the ground to observe these wavelengths. However, for shorter wavelengths, from sub-millimeter to centimeter scales, observations are typically conducted from carefully chosen high-altitude, dry, and cold sites to minimize atmospheric interference. This accessibility to the sky from Earth is also a notable feature shared with telescopes operating in the visible to near-infrared range.

When two antenna dishes observe an object in the sky, they view it from slightly different positions. This results in the light from the object reaching one antenna before the other. By precisely timing and correlating the signals from each antenna, astronomers combine these signals without interference—a technique known as interferometry.

The imaging process in a radio interferometer involves combining the fringe patterns produced by all pairs of baselines between the antennas. Each baseline measures the visibility function at distinct points in the UV plane, which corresponds to the projected baseline vectors. This visibility is essentially the Fourier transform of the intensity

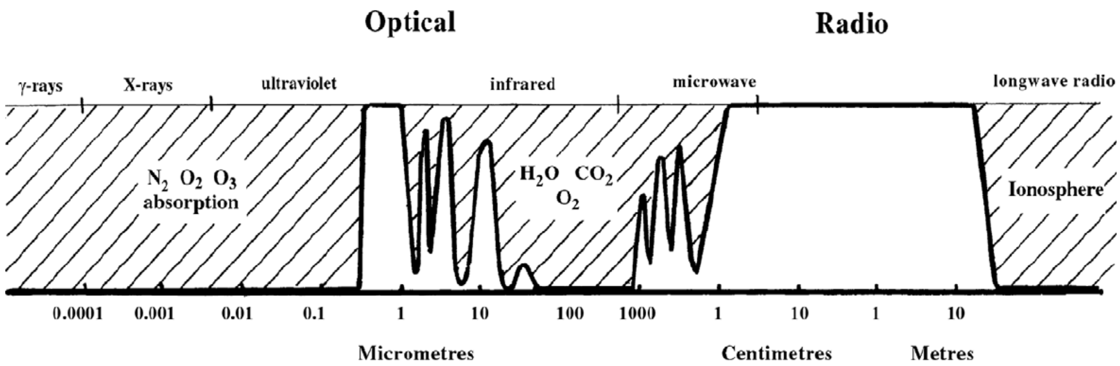

Figure 2.1.: The electromagnetic spectrum showing the atmospheric opacity. The radio range is limited by the ionosphere at wavelengths greater than a few metres, and by molecular absorption in the sub-millimetre range. [5]

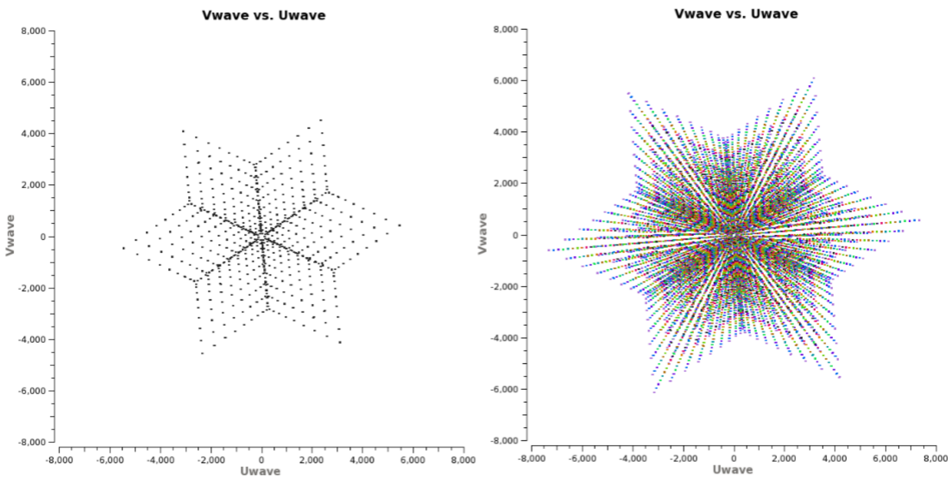

Figure 2.2.: Baselines are vectors in (u,v) plane. Left: (u,v) coverage snapshot at a single frequency. Right: Multi-Frequency snapshot of (u,v) coverage. [6]

distribution of the source. To achieve a smooth reconstruction of the intensity distribution, or the image, it is crucial to obtain visibility measurements across various baselines. The rotation of the Earth, combined with the assumption that the source remains stationary throughout the observation, enhances baseline sampling. By adjusting parameters such as baseline length and signal frequency, the resolution and sensitivity of the interferometer can be tailored to meet specific research goals.

According to the van Cittert–Zernike theorem, all information about the source's intensity, $f(x, y)$, is encoded in the two-point correlation function $F(u, v)$ across the incoming wavefront. This correlation function is obtained through pairwise measurements by the antennas in the interferometer array. The $F(u, v)$ is the Fourier Transform of $f(x, y)$. Here, (u, v) are the components of the projected baseline vector expressed in units of wavelength. Essentially, $F(u, v)$ quantifies the frequency at which sinusoidal features of the source structure repeat over a given distance.

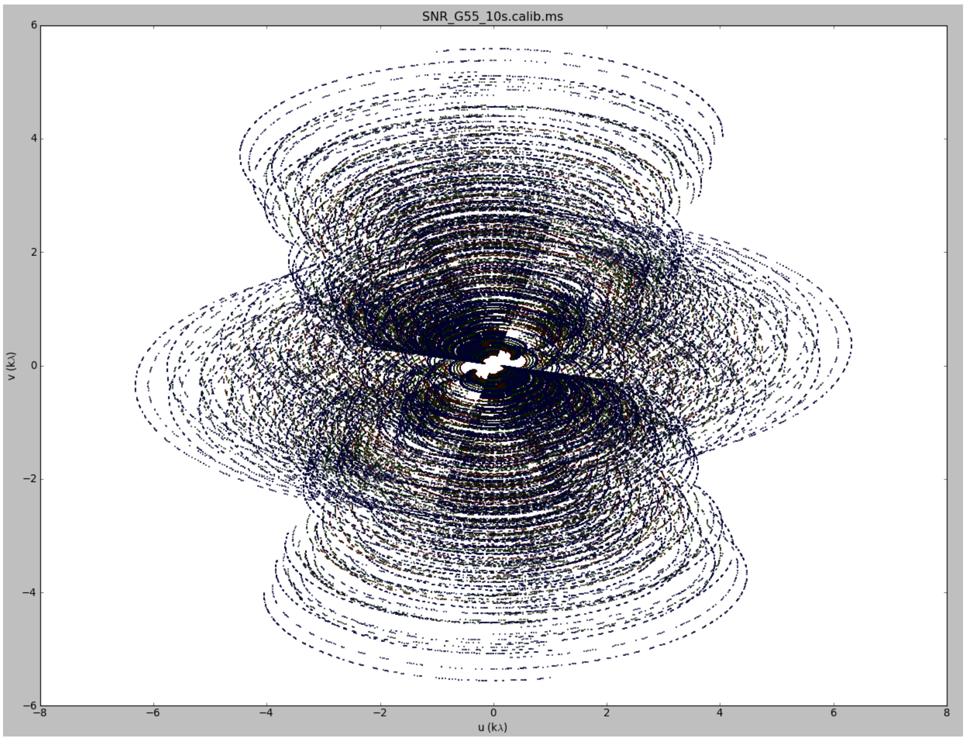

Figure 2.3.: Sampling Function for the above Baselines, (u,v) coverage for the 8-hour observation. Visibilities are sampled from the sampling function. [6]

Interferometers can therefore achieve high precision by using multiple smaller antennas instead of a single large one. The visibilities captured by these antennas are later transformed into sky brightness through Fourier transformation. The configuration of baselines affects the resulting image: smaller baselines provide better sensitivity, while larger baselines yield higher angular resolution. [9] [15]

2.2. Data Processing

To process the visibility data from the interferometer specialized software packages are used such as CASA (Common Astronomy Software Applications). Before imaging, the data undergoes flagging to remove Radio Frequency Interference (RFI) and other spurious disturbances. Several calibration steps follow, such as prior calibration, flux calibration, bandpass calibration, and gain calibration.

Once calibrated, the visibility data is gridded in the UV plane for Fourier transformation. The resulting image, called a **dirty image**, contains artifacts from the incomplete UV sampling and the antenna's point spread function. To clean up these artifacts, a deconvolution algorithm like **CLEAN** is used. The CLEAN algorithm iteratively subtracts the brightest point sources from the dirty map, constructing a model of the sources until a defined threshold is reached (based on either the number of iterations or the residual image approaching the noise level).

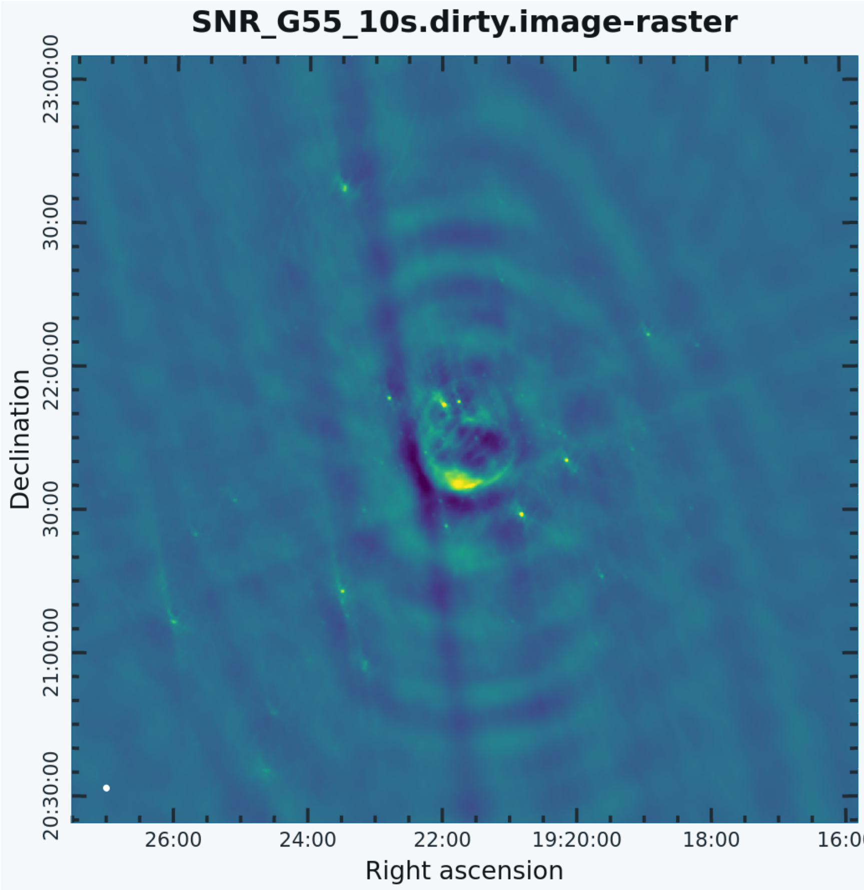

Figure 2.4.: Dirty Image for the source. Dirty image is the fourier transform of sampled visibilities, and the convolution of Dirty Beam (Fourier transform of point spread function) and some residual artifacts [6]

After this deconvolution, the brightness distribution can undergo further refinement through self-calibration. In self-calibration, the brightness distribution is used as a model to recalibrate the phase and amplitude of the data. When the signal-to-noise ratio (SNR) is high enough, self-calibration yields much better results, as it allows for phase and gain calibration from within the same region of the observed sky, rather than relying on distinct, external calibrators.

CASA (Common Astronomy Software Applications) is a versatile tool designed for the processing of radio interferometric data from both single-dish and aperture-synthesis telescopes. It is essential for data reduction and imaging pipelines, allowing astronomers to extract meaningful information from their observations. Figure 2.6 outlines the sequences of processes in CASA.

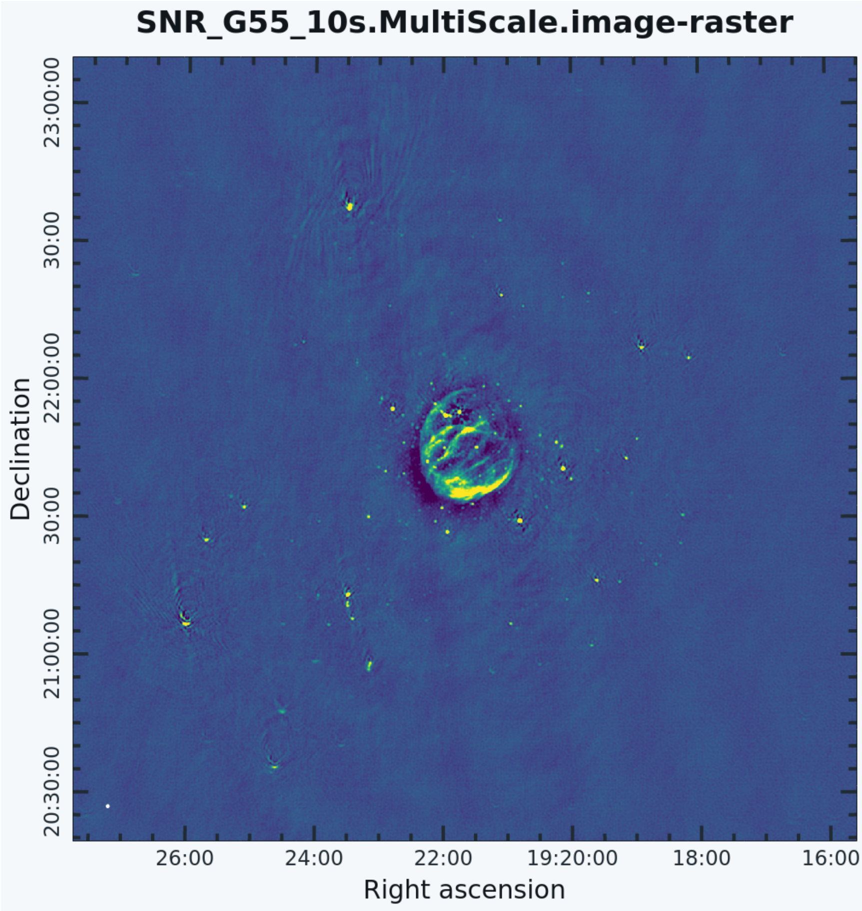

Figure 2.5.: Clean Image obtained after applying Multi-Scale Clean. Clean image is the sky brightness distribution we receive after applying the iterative CLEAN algorithm. [6]

However, the massive datasets generated by modern interferometers, such as the MeerKAT telescope in the Karoo desert, require more advanced processing techniques than traditional serialized approaches. To meet these needs, the Automated Radio Telescope Imaging Pipeline (ARTIP) was developed. [8] This pipeline, which will be detailed in the next section, automates much of the data processing and is optimized for handling large volumes of interferometric data efficiently.

2.3. ARTIP

MALS generates vast amounts of data, which necessitated the creation of a specialized data processing tool—the Automated Radio Telescope Imaging Pipeline (ARTIP). Traditional serialized data processing approaches are insufficient to handle the immense data volume produced by MALS. As a result, ARTIP was developed (as detailed in the the publication [8]) to automate and streamline the process. This pipeline is specifically designed to handle the complexities of large-scale radio interferometric data and ensures that the

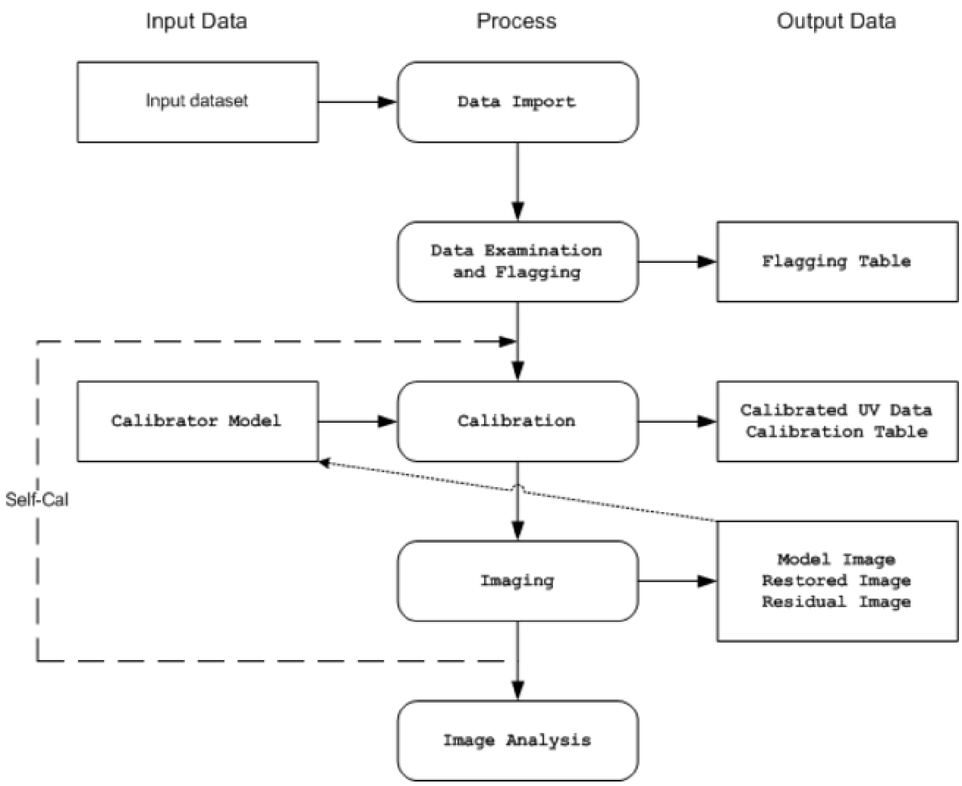

Figure 2.6.: CASA Workflow [7]

MALS data are processed efficiently. ARTIP is built using Python 3.6 and extensively leverages tools and tasks from the Common Astronomy Software Applications (CASA) package, which is a widely used software suite for processing radio astronomical data as described above.

One of the key features of ARTIP is its scalability and adaptability. It is deployed on the VROOM computing cluster at the Inter-University Centre for Astronomy and Astrophysics (IUCAA). This cluster-based implementation allows ARTIP to process large volumes of data in parallel, which is essential given the geographic distribution of the MALS team. By enabling collaborative data processing, ARTIP allows different members of the research team to work simultaneously on different parts of the dataset, thus improving overall efficiency and reducing the time required for data analysis.

ARTIP plays a critical role in converting raw MALS data into scientifically useful outputs. Its primary function is to process the data and generate full-Stokes radio continuum images along with spectral line cubes. These outputs are crucial for analyzing the structure and characteristics of radio sources in the MALS catalog. Although ARTIP was originally developed for the specific needs of MALS, it is versatile enough to be applied to other radio interferometric datasets. For instance, ARTIP can process data from major radio

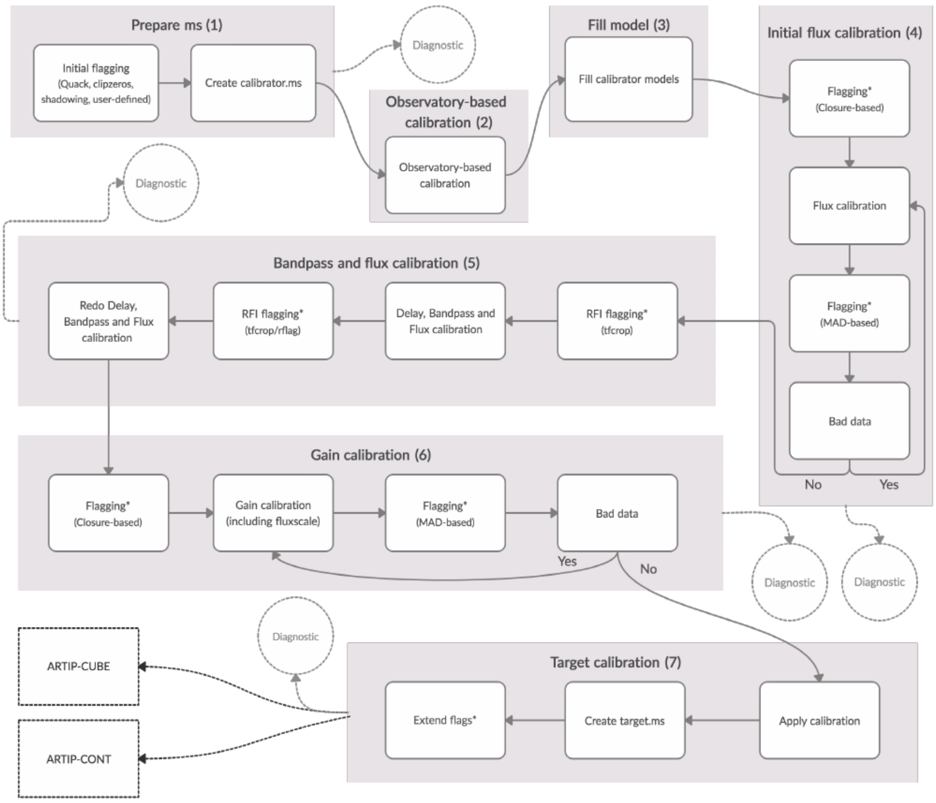

Figure 2.7.: ARTIP CAL[8]

telescopes such as the Very Large Array (VLA) and the upgraded Giant Metrewave Radio Telescope (uGMRT). This adaptability makes ARTIP a valuable tool not only for MALS but also for future surveys and projects that rely on radio interferometry.

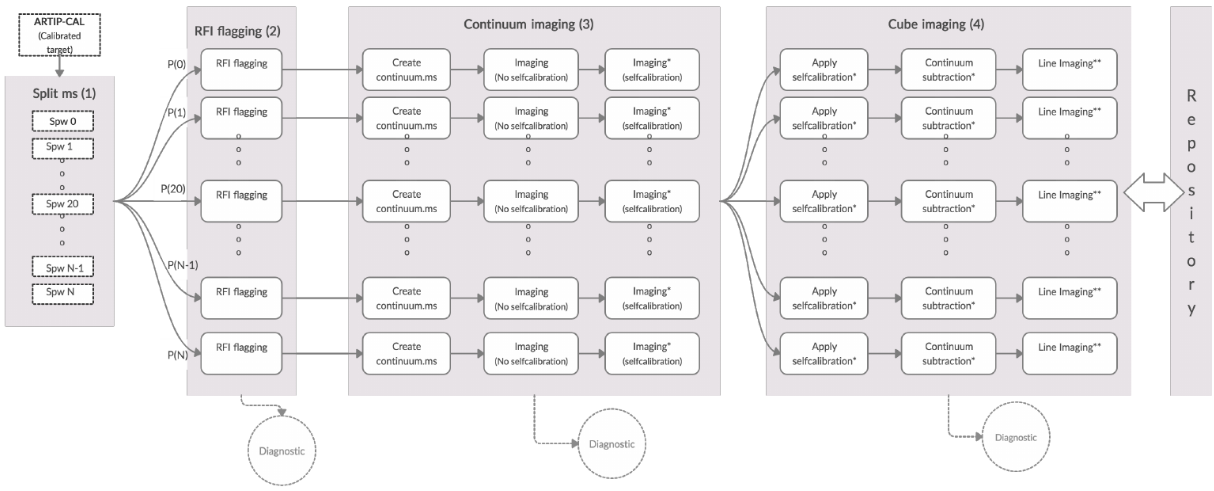

Figure 2.8.: ARTIP CUBE[8]

In this study, ARTIP was used to preprocess all the spectral data collected for MALS sources. The pipeline consists of two main processing units: ARTIP-CAL and ARTIP-CUBE, which handle different aspects of the data processing workflow. Figure 2.7 illustrates the calibration unit, ARTIP-CAL, which performs the necessary corrections and calibrations on the raw data. Figure 2.8 shows ARTIP-CUBE, which is responsible for generating the final spectral line cubes used for scientific analysis.

2.4. Radio Overlays

To further investigate the overlap between galaxies and any potential radio sources present behind them (i.e., galaxies in the line of sight of radio sources), a method was developed to generate radio overlays of these sources over the visible images of the galaxies. This approach served as a visual aid to narrow down the number of candidate sources that might show HI absorption signatures in their spectra.

For this purpose, the catalog from MW23 [16] was used to assign morphological classifications to objects identified in the DESI Legacy Survey. Accordingly, the same DESI DR8 image cutouts were employed for the visible component of the images since the MW23 model was trained on DR8. The radio overlays were created using data from MALS-DR1v2.

The visible image cutouts had a field of view (FoV) of 134.1 arcseconds, while the radio overlays had a significantly larger FoV of 500 arcseconds, which is the maximum FoV available from these surveys. The radio contours used for these overlays were defined at specific signal-to-noise ratio (SNR) levels of [-1, 1, 3, 5, 10, 17], allowing for a clear representation of radio emission intensity.

All the overlay plots were centered on galaxies identified in the DESI Legacy Survey, ensuring consistent alignment between the radio and visible components. Figure 2.9 presents some examples of these radio-visible overlay plots, showcasing the integration of radio emission data with the optical morphology of galaxies.

If we could find some instances where the radio contours overlap the visible image of galaxy, we have a case of galaxy interviewing the radiation from the radio source. These are shown in Figure 2.10.

These radio overlay plots were used in both the investigation in chapter 4 and 5.

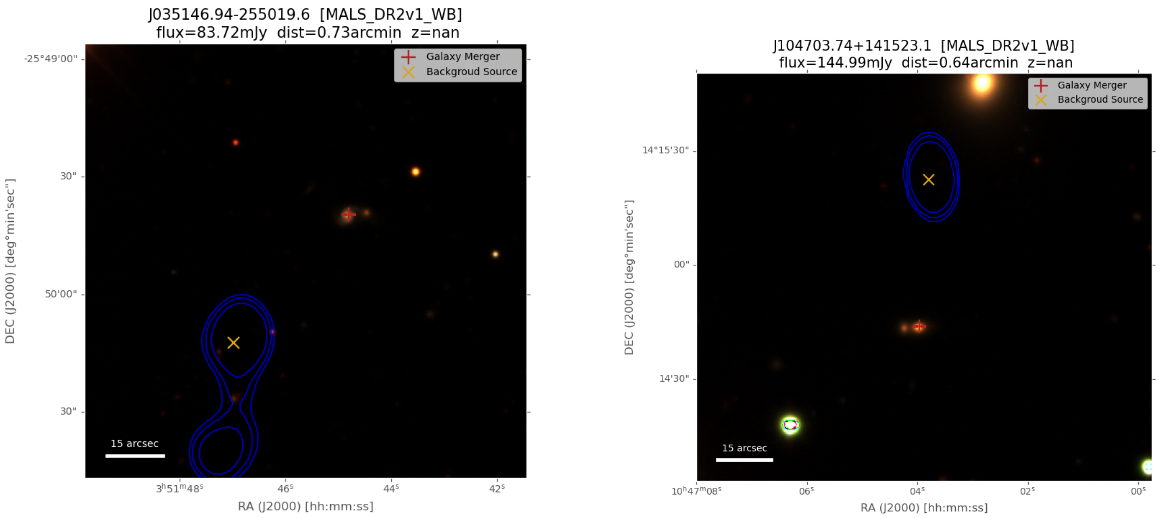

Figure 2.9.: Visible image cutouts with non-overlapping radio contours

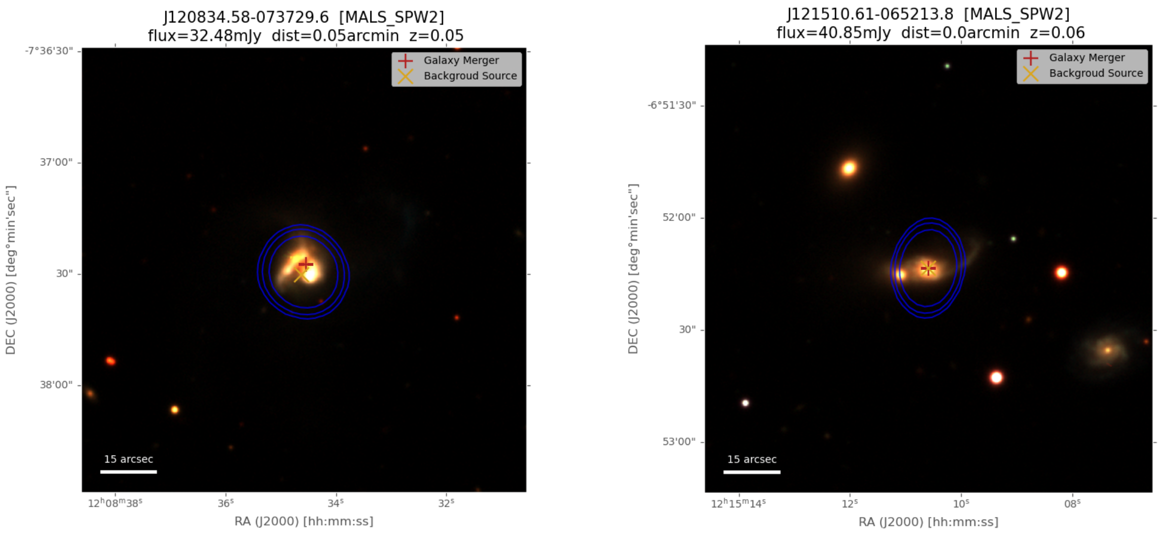

Figure 2.10.: Visible image cutouts with overlapping radio contours

CHAPTER 3

MEERKAT ABSORPTION LINE SURVEY

3.1. Survey Overview

The Square Kilometer Array (SKA) is poised to revolutionize radio astronomy, emerging as the world's largest and most sensitive radio telescope. At its highest operational frequencies and longest baselines, the SKAO is expected to achieve sub-arcsecond resolution. The construction phase involves deploying 133 antennas, each 15 meters in diameter, in South Africa, and 131,072 log-periodic antennas in Australia. Until the completion of SKAO Phase-I, the MeerKAT radio telescope will remain the most sensitive instrument operating at centimeter wavelengths. MeerKAT, one of the four precursor telescopes to the final SKA, comprises 64 antennas, each with a 13.5-meter dish, located in South Africa. [17]

MeerKAT plays a pivotal role in the MeerKAT Absorption Line Survey (MALS), a project dedicated to investigating HI 21-cm and OH 18-cm absorption lines within the redshift range $0 \leq z \leq 2$. This range covers critical epochs of cosmic history where the star formation rate (SFR) density experiences steep evolution. The absorption lines probed by MALS allow us to study the physical conditions in the cold phases of the interstellar medium (ISM), yielding valuable insights into the galaxy evolution, star formation rates, and the role of cold gas in shaping the universe's structure over cosmic time. Observations from MALS provide critical measurements of the evolution of cold atomic and molecular gas cross-sections in galaxies and offer an unbiased census of HI and OH absorbers. In parallel, MALS conducts blind surveys for HI and OH emission lines and a radio continuum survey, adding substantial value to its scientific goals. [14]

MALS has been allocated a total of 1655 hours of observational time on MeerKAT, covering both L and UHF bands. The L-band ranges from 900 MHz to 1670 MHz, while the UHF band spans from 580 MHz to 1015 MHz. Observations include 740 pointings in the L-band and 370 pointings in the UHF band, with cumulative on-source times of 691 hours and 746 hours, respectively. The 1100 MALS pointings employ 32,768 frequency channels, observing in both parallel and cross-parallel polarization modes. With a correlator dump time of 8 seconds, each pointing generates approximately 1 TB of data per hour. Over the entire observation period, this results in a raw visibility data volume of around 1.7 petabytes (PB).

3.2. Data Products

3.2.1. MALS-DR1v2

MALS Data Release 1 provides high-quality L-band continuum images for two specific spectral windows (SPWs) within the broader MeerKAT radio telescope's capabilities: SPW2 (976.4–1036.5 MHz) and SPW9 (1350.9–1411.0 MHz). As part of a larger survey effort, MALS recently completed a series of 391 L-band pointings, covering a frequency range of 900–1670 MHz. These pointings specifically targeted sources with declinations $\delta \leq +20°$, ensuring a broad sky coverage for the study of extragalactic radio sources. Each pointing had an on-target observation time of 40 minutes, centered on radio sources brighter than approximately 200 mJy at 1 GHz. The observations were carried out using the MeerKAT 64-dish array in 32K channel mode, producing spectral line cubes with a high velocity resolution of approximately $\sim 6.1\,\mathrm{km/s}$. [18]

These observations enable detailed studies of radio sources with brightness levels exceeding $\sim 1\,\mathrm{mJy}$, specifically focusing on detecting HI 21-cm and OH 18-cm absorption lines. These lines are of particular interest for studying the neutral and molecular gas content in galaxies. For HI 21-cm absorption, MALS is capable of probing sources within the redshift range $0 \leq z \leq 1.4$, while for OH 18-cm absorption, the redshift coverage extends to $0 \leq z \leq 1.9$. This redshift range allows for a comprehensive exploration of both nearby and distant galaxies, providing insights into their gas reservoirs and the physical processes at play.

The accuracy of the MALS catalog is notable, with a flux density scale precision of better than 6%, and a scatter of approximately 15%. Additionally, the astrometric precision is highly reliable, with positional accuracy within 0.8 arcseconds. These factors make the MALS data valuable for a range of astrophysical studies, from galaxy evolution to the detection of distant quasars. The catalogs and images are publicly accessible, ensuring that the data can be utilized by the broader scientific community for further research (https://mals.iucaa.in).

In future phases, MALS will focus on observations within the UHF band (580–1015 MHz), which is complementary to the L-band data. For these upcoming observations, the spectral band will be divided into 15 spectral windows (SPWs), labeled SPW0 through SPW14, to cover a wide frequency range. This expanded frequency coverage will provide even greater sensitivity and allow for a broader exploration of astrophysical phenomena in both nearby and distant galaxies.

3.3. Case Study: L-band Focus

For this thesis, we focused primarily on L-band observations, with a redshift range of $z < 0.6$. Special emphasis was placed on the lower redshift range, $z < 0.1$, to enable more detailed studies of individual galaxies and their gas properties. Within the L band, we specifically examined two spectral windows (SPWs): SPW2, covering the frequency range 976.4–1036.5 MHz, and SPW9, which spans 1350.9–1411.0 MHz. These spectral windows were chosen to allow for detailed analysis of both HI emission and absorption features in nearby galaxies, providing insights into the cold gas content and dynamics at low redshifts.

An sample of the processed spectrum from ARTIP for a source identified via galaxy mergers (as discussed in Chapter 4) is shown below.

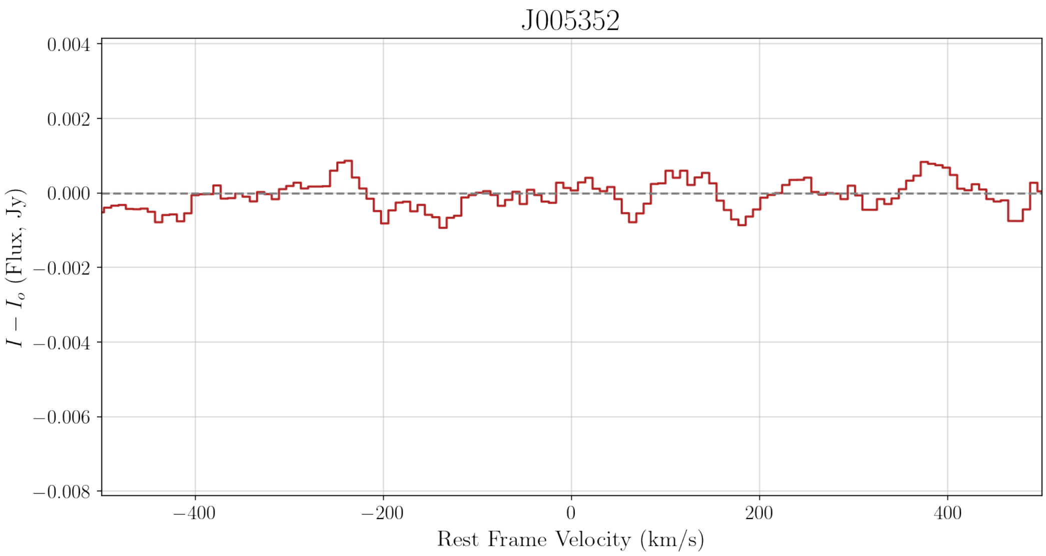

Figure 3.1.: Spectrum of the source J005352 taken after ARTIP processing, and smoothed over five consecutive spectral widths

CHAPTER 4

IDENTIFYING GALAXY MERGERS

Our primary objective in this study was to observe the absorption signatures of the HI 21-cm line in the spectra of sources from the MeerKAT Absorption Line Survey (MALS). To achieve this, we employed two main approaches. The first involves identifying objects of interest that are likely to produce an absorption signature. This can include searching for gas clouds, galaxies intervening in the line of sight of a background source, or even associated absorption signatures at the source itself. This chapter will elaborate on our efforts to locate these objects of interest, focusing specifically on galaxy mergers. The second method—searching for absorption signatures directly in the source's spectra—will be detailed chapter 5.

The choice to concentrate on merger events for our initial investigations, rather than other astrophysical phenomena, is driven by their significant role in triggering the collapse of cold neutral and molecular gas within the interstellar medium (ISM). Such collapses often lead to the formation of star-forming regions, making mergers critical for understanding star formation processes in galaxies. [19]

Mergers are dynamic events that stimulate star formation within galaxies. When two galaxies interact, their gravitational forces can disturb gas distributions, causing compression and triggering the formation of new stars. This process can significantly enhance the star formation rate (SFR) in the merging galaxies, providing a unique opportunity to study the connection between cold gas dynamics and star formation. By focusing on galaxy mergers, we can gain valuable insights into the complex interplay between gas dynamics, star formation, and galaxy evolution.

4.1. Galaxy Zoo DESI Catalogue

The Dark Energy Spectroscopic Instrument (DESI) Legacy Survey is a comprehensive optical/infrared spectroscopic survey primarily targeting the North Galactic Cap (NGC) and the South Galactic Cap (SGC). It integrates data from various individual imaging projects conducted on different telescopes, including the Mazin's Legacy Survey (MzLS), the DECaLS (Decadal Survey of the Milky Way), and the BASS (Baryon Oscillation Spectroscopic Survey). The DECaLS Survey encompasses data from the g, r, and z bands, while BASS focuses on the g and r bands, and MzLS solely utilizes the z band. Starting from Data Release 10 (DR10) onwards, the Legacy Surveys are extending their coverage to include the i bands from DECaLS and NEOWISE. Photometric measurements are derived from the flux densities obtained in these bands. Alongside calibrated images, the project delivers a catalog designed to estimate source shapes, brightnesses, and also redshifts, providing a valuable resource for further astronomical investigations[20].

The primary objective of the Galaxy Zoo project is the morphological classification of galaxies observed in astronomical images. This classification holds significant importance in astronomy as it provides valuable insights into the formation, evolution, and properties of galaxies, including their star formation activity, dynamical history, and interactions with other galaxies. The Galaxy Zoo project engages volunteers in the classification process by presenting them with images of galaxies sourced from large-scale surveys conducted by telescopes like the Sloan Digital Sky Survey (SDSS) and the Hubble Space Telescope. Volunteers visually inspect these images and categorize the galaxies based on their morphological features, such as whether they exhibit spiral, elliptical, irregular, or merger characteristics.

The work conducted by Walmsley et al.[16] (hereafter referred to as MW23) has been pivotal to the progression of our project. Their study involved training a machine learning model using morphology classifications provided by volunteers from Galaxy Zoo on select DESI images. Subsequently, this model was utilized to assess the morphology of an impressive 8.67 million galaxies. Without the assistance of machine learning, achieving such a feat through volunteer efforts alone would have required approximately 200 years. The measurements derived from this model encompass various morphological features of galaxies, including the presence of bars (strong, weak, or none), spiral arms (along with their count and winding), and indications of recent mergers.

By training on a set of 33 labels, MW23 generated a catalogue of objects with vote fractions ranging from 0 to 1 for all labels. This model typically predicts the fraction of volunteers selecting each answer with an accuracy of 5-10% for every question posed by the Galaxy Zoo. The final models trained on a dataset consisting of 401,000 galaxies labeled with 10 million volunteer classifications.

The MW23 catalogue was used to identify objects within 45 arcminutes of the MALS pointing centers. A total of 17,113 recognizable objects were found within the 391 MALS L-band pointing centers, as described in Chapter 1. Notably, 157 out of the 391 pointings did not yield any sources, as they fell outside the coverage area of DESI.

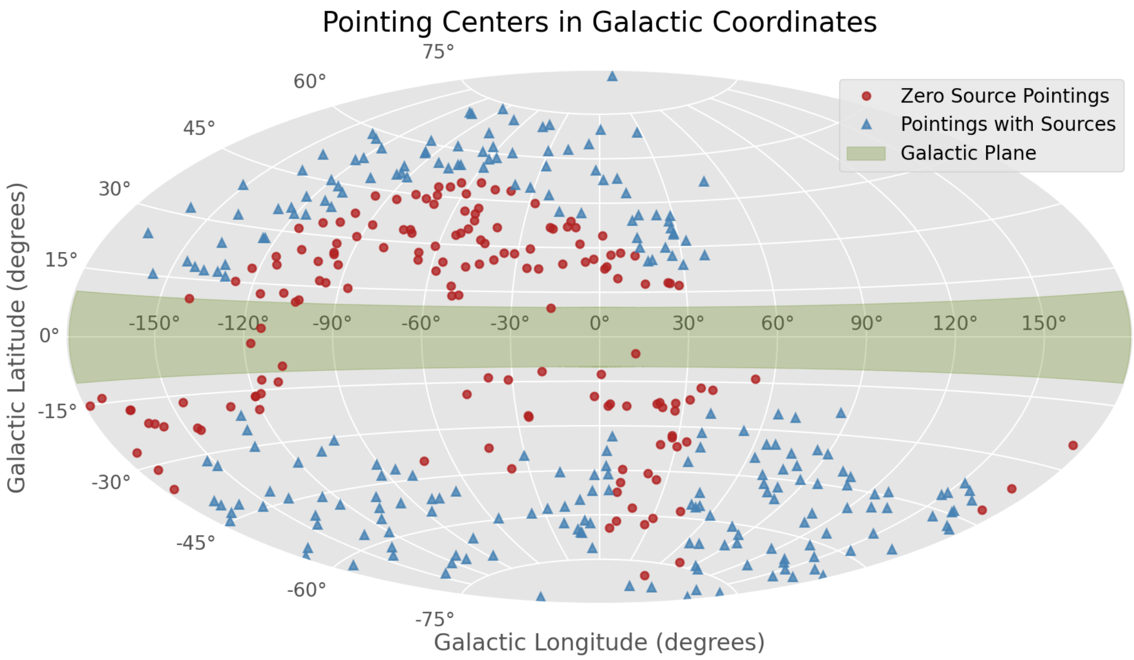

Figure 4.1.: 391 pointing centres in MALS L-band

All 17,113 objects consisted of galaxies with assigned weights for different labels or categorizations, ranging from 0 to 1. These labels correspond to questions posed to volunteers during the classification process. For example, questions include "Is this galaxy smooth or disk-featured?", "Does this galaxy have a disk edge on (yes)?", "Does this galaxy have a large bulge size?", "Does this galaxy have 4 spiral arms?", and "Does this galaxy show signs of merging?". A weight of 0.45, for instance, indicates that 45% of volunteers selected 'yes' for the question "Does this galaxy show signs of merging?".

Among the various categorizations available, the labels related to merger events appeared particularly promising due to their direct relevance to our study. We specifically targeted the label "Does this galaxy show signs of merging?" as it directly indicates the presence of a significant merger event, likely to have a profound impact on the ISM and subsequent star formation activity. By selecting galaxies with the highest vote fraction for this label, we aimed to identify the most prominent merger candidates within our dataset.

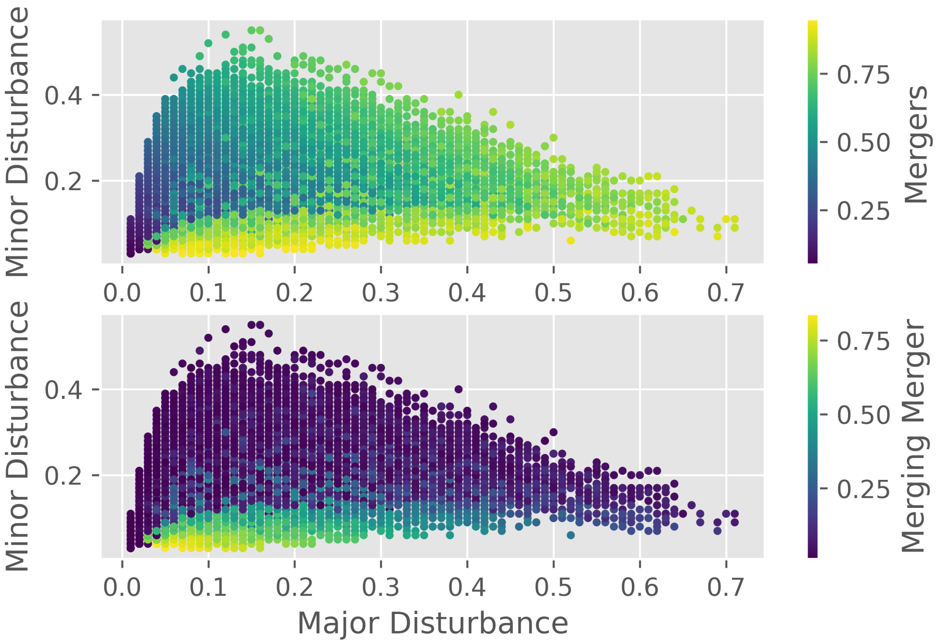

Figure 4.2.: Four merger labels by their vote fraction

4.2. Analysis of 109 Mergers

Since we cannot analysis the large pool 17,113 objects individually, setting a threshold vote fraction > 0.76 for the merger label allowed us to narrow down our selection to 109 potential merger candidates. This threshold was chosen to ensure a sufficiently high confidence level in the merger classification while retaining a sizable sample for specific analysis.

Next, we identified radio sources situated behind the line of sight of the merger events. To accomplish this, we utilized data from the MALS-DR1 catalogue on radio sources[18]. For each of the 109 identified merger events, we identified the nearest sources with flux densities greater than 1 mJy using their (RA, Dec) coordinates.

Our objective was to find instances where the radio contours overlap with the visible images of the merger events. In order for the absorption spectrum to be worth investigating, the peak flux of the background radio source should also ideally be around 5 mJy (at least 4 mJy).

Applying thresholds for both source brightness and angular proximity between the source and mergers, we set conditions that the peak flux should exceed 5 mJy and the separation between the merger and source should be less than 2.5 arcminutes. Initially, we identified 13 potential merger-source pairs. However, upon closer examination, none of these pairs exhibited overlapping radio contours with a peak flux greater than 5 mJy. This outcome indicates that, unfortunately, no suitable merger-source pairs meeting our criteria were identified for further investigation.

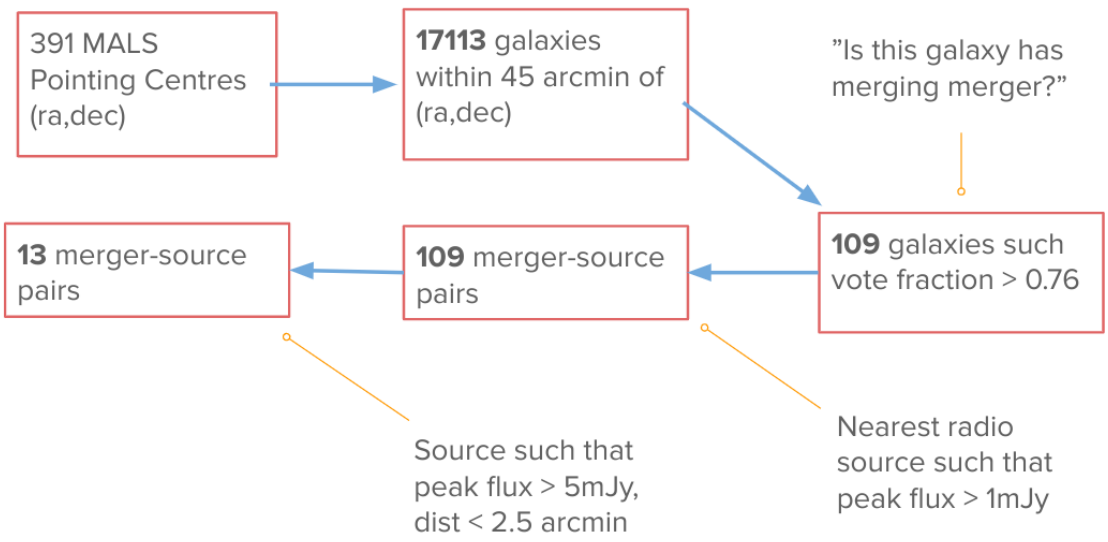

Figure 4.3.: Progression of analysis for one label

4.3. Considering all labels

To better constrain the large number of object-source pairs found in our study, we applied some stringent filters to the initial database of 17,113 objects, focusing not only on merger morphology but on all available labels. Our objective was to narrow down to a group of approximately 50 pairs for further individual analysis to verify the accuracy of our procedures.

We identified a total of 49 source-object pairs by applying the following filters:

- **Peak flux density of sources $>$ 30 mJy**: Background sources need to have appreciable flux density to produce an identifiable absorption spectrum.
- **Angular distance between source and object $<$ 1 arcmin**: We aimed for the radio contours of sources to overlap with the visible image of the object, increasing the likelihood of detecting absorption signals along the line of sight.

- **Vote fraction for the label "Does this galaxy show signs of a merging merger?" > 0.4**: Merger events are good indicators of cold neutral gas extending beyond the optical diameters of galaxies.

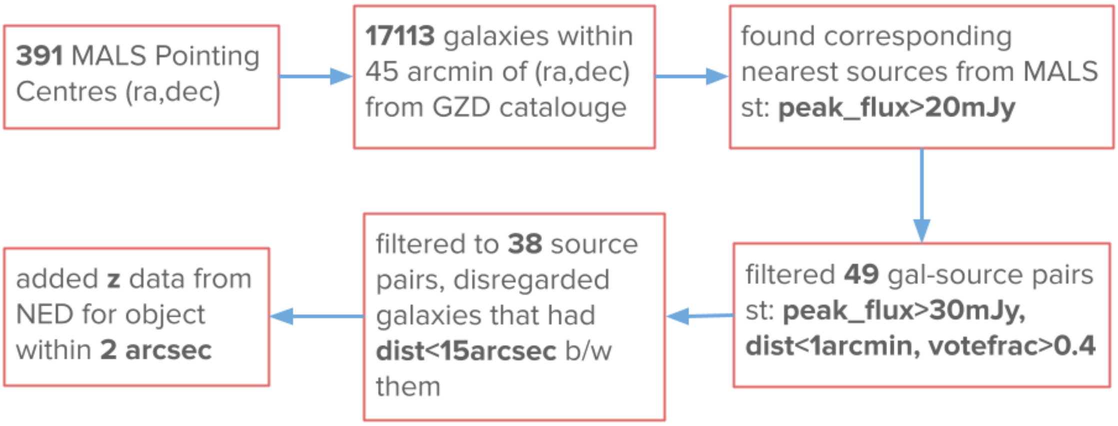

Figure 4.4.: Progression of analysis for all labels

Within the selection of 49 pairs, we found instances of duplicate merger coordinates in the GalaxyZooDESI (GZD) database. We ultimately obtained 38 unique source-object pairs for further analysis by disregarding the one of the objects in the duplication.

Out of the 38 source-merger pairs there were only 9 sources that had their redshift data available on NED (NASA/IPAC Extragalactic Database). These redshift data were added to the table for the objects identified within 2 arcseconds from NED. (Table 4.1)

4.4. Calculation for GZD-MALS Sources

Spectra for the nine sources with redshift data available in NED were obtained from the MALS data after ARTIP pre-processing. Only the sections containing the redshifted frequency (observed frequency) within the corresponding spectral window (SPW) were considered, as described in [8]. Details of these sources are provided in Table 4.1, where `source_name` corresponds to the source names in MALS_DR1_V2.

The flux data was processed using boxcar smoothing over five spectral widths. One source, J224757.33+032525.6, was excluded from the analysis as its observed frequency fell within a region flagged for radio frequency interference (RFI) in the MALS data. This left us with a total of eight sources for further analysis.

In our analysis, we considered the speed of light, $c = 299792.458\,\text{km/s}$, and the rest frequency of neutral hydrogen, $\nu_{rest}^{HI} = 1420.405752\,\text{MHz}$. The heliocentric frequencies from the data were converted to rest frame velocities using, $v = c\left(\nu_{obs}^{HI} - \nu\right)/\nu_{obs}^{HI}$, where ν_{obs}^{HI} is the observed frequency. [21] This conversion allows for the comparison of spectral features in the rest frame of the sources.

Following this, a velocity range of $-200\,\text{km/s}$ to $200\,\text{km/s}$ around the optical redshift of the merger was considered to fit a Gaussian to the spectrum. Unfortunately, none of the sources showed a detection of the HI absorption feature.

This result indicated that the initial procedure of identifying galaxy morphologies and then examining the corresponding source spectra was ineffective. Even after expanding the selection to include all galaxies in the catalog, rather than focusing solely on indicators of star formation such as merging galaxies, we were unable to find any galaxy-source pairs that met our specified thresholds and exhibited an absorption signature in their radio source spectra. As a consequence, we had to adopt a different approach to identify absorption features, which will be detailed later in Chapter 5.

From the non-detections in these 8 sources, we could calculate the non-detection upper limits for integrated optical depth and column density. We considered the rms value (σ_I) of flux to be the median of rms flux values in the 400 km/s range around the optical redshift. A 5σ limit for τ_{rms} were assumed for the non-detected line profile;

$$\tau_{lim} < \frac{5\sigma_I}{I_o}$$

where I_o is the peak flux of the source. Similarly, for a FWHM of 100 km/s, the upper limits to integrated optical depth were found by;

$$\int \tau\delta v < \tau_{lim}\delta v \left(\frac{2.54 \times \text{FWHM}}{\Delta v}\right)^{-1/2}$$

Furthermore, for an assumed spin temperature of 100 K, the column density upper limits were calculated as;

$$N(HI) < 1.823 \times 10^{18} \times T_s \int \tau\delta v$$

The upper limit values for these 8 sources is given in Table 4.2.

Plots for the continuum-subtracted flux within 500 km/s around the observed HI frequency are given in Appendix B.

Source Name	Peak Flux (mJy)	RA (deg)	DEC (deg)	Vote Frac	Redshift	HI Freq (obs)	SPW	RFI Flag
J005352.37+172720.8	157.34951233360002	13.466450699583552	17.450460026169008	0.45	0.406594	1009.8192882949876	2	0
J011826.65-203752.8	54.24351354819	19.61135297556665	-20.63161146891509	0.44				
J021443.83+174659.5	93.28902593457	33.68264235310412	17.783207131160427	0.62	0.143923	1241.696995339721	6	0
J024925.73-074602.8	54.89360748032001	42.35780603711164	-7.768030601497459	0.42	0.417597	1001.9813473081559	2	0
J025045.30-071855.2	30.462923387950006	42.689604541979854	-7.316592522974019	0.5				
J033908.88-224705.6	33.89875776951	54.78759845297935	-22.78544727012518	0.5				
J035146.94-255019.6	83.72351445797	57.94583096026992	-25.83684119560109	0.63				
J035508.35-080340.2	44.71548612703001	58.78524850364113	-8.06168228238245	0.48	0.243626	1142.1486459755586	5	0
J044754.37-093813.7	33.42885222448	71.97655171486944	-9.63712632441967	0.72				
J055954.58-254320.5	36.90459083135	89.9774334486121	-25.72237255052866	0.41				
J075006.72+270023.1	353.14740234318003	117.52956120546504	27.00612948345349	0.56				
J080116.77+074831.3	41.13648422368	120.3204335678832	7.808134223102679	0.43				
J095414.87+003306.3	140.52336219328998	148.56219674925214	0.55145206902565	0.5				
J104703.74+141523.1	144.99227348113	161.76587113020813	14.25614308154216	0.72				
J112724.41-074553.0	136.30404047118998	171.85155350266265	-7.764694739182019	0.57				
J113212.50+053455.2	110.48077278285	173.054738371016	5.58157579828952	0.68				
J120514.13-070839.3	30.10490967181	181.308214839858	-7.15256558249535	0.56	0.131378	1255.4652397342002	7	0
J120834.60-073728.5	41.79922110703	182.14416035110668	-7.62458549501931	0.49	0.049771	1353.0624793407324	9	0
J121510.60-065213.6	34.87112618961	183.79445501772344	-6.870729106589071	0.54				
J121903.42-071437.3	105.52683129861	184.7652973989959	-7.2423276147412095	0.52				
J125223.26-040525.0	32.265147598789994	193.0975983994795	-4.09054898007909	0.49				
J164058.75+114403.9	297.12291013008	250.2458209484412	11.73377306360728	0.68				
J163958.57+111041.0	66.78384392325	249.99460857926843	11.177506938169438	0.53				
J164058.75+114403.9	297.12291013008	250.2458209484412	11.73377306360728	0.68				
J212042.40+132725.3	383.20632341584	320.17722292817894	13.45647437670558	0.43				
J222252.96+121350.1	280.37236623491003	335.720972446108	12.23030163908373	0.48				
J223826.45-134421.7	160.08347966677	339.610461428906	-13.739755876975927	0.41				
J224653.53+180324.1	45.57392324520001	341.7231267462314	18.05641805835877	0.49				
J224757.33+032525.6	43.1309115103	341.9888934370257	3.42378477538128	0.41	0.124742	1262.872509428829	7	1
J230055.50+064544.0	119.39192098901	345.2317766300708	6.76342048398934	0.58	0.257	1129.9966205250594	4	0
J005022.24-572532.9	31.011751612790004	12.599075155695813	-57.42803541766327	0.68	0.33609	1063.106341638662	3	1
J005319.51-574300.0	43.06836241814	13.331277371503198	-57.71664447798135	0.53				
J005139.21-570804.1	56.60262054551	12.91336765774697	-57.13447869311013	0.56				
J004842.35-581707.7	140.65611084884	12.17667827783873	-58.28568703126508	0.43				
J033443.67-521901.3	42.09814958975	53.68283670060461	-52.31753926786526	0.52				
J032918.33-512053.4	37.67404400028	52.32724604117697	-51.34872160664575	0.47				
J213024.35-434818.9	337.00414607411	322.60144193537604	-43.80525318852051	0.5				
J231433.13-435714.2	336.30287234576	348.63893891822204	-43.954405789819496	0.5				

Table 4.1.: Selection of 38 source-object pairs with their properties.

Source Code	δv **(km/s)**	σ_I **(Jy/b)**	τ_{lim}	$\int \tau \delta v$ **(km/s)**	N(HI) $\times 10^{18}$ **(cm^{-2})**
J005022	7.366880310592251	0.0007797982187666	0.0001257262454090133	0.0054385686084108854	0.9914510573133044
J005352	7.75481507180811	0.0008836809521221001	2.808019354545534e-05	0.0012462428453302633	0.22719007070370698
J021443	6.306546508237943	0.00171285932202	9.180390216644271e-05	0.0036742931337061784	0.6698236382746363
J024925	7.815506665634558	0.0007782500974433	7.08871335995099e-05	0.0031583688139545938	0.5757706347839224
J035508	6.856299942755641	0.0009457416194295	0.00010575101618517458	0.004413125843241846	0.8045128412229884
J120514	6.2381344253107045	0.00124018479872675	0.00020597716655633238	0.008199045613531039	1.4946860153467083
J120834	5.788173902842232	0.0007674504414939	9.180200266516765e-05	0.0035199767846031296	0.6416917678331505
J224757	6.2010020225948494	0.0018503530578917	0.00021450428394607674	0.008513022179292217	1.5519239432849712
J230055	6.930156790313788	0.0007959320086816	3.3332741532606103e-05	0.0013984901866385452	0.25494476102420677

Table 4.2.: Calculation for 8 source-object pairs.

4.5. Conclusion

In this chapter, we presented our efforts to search for absorption signatures in radio source spectra by initially focusing on promising candidates, specifically merging galaxies. The classification of these galaxies was based on a morphology catalog developed by [16]. Their work utilized a machine learning model trained on labels provided by citizen scientists through the Galaxy Zoo project. In this project, image cutouts of objects identified by the Tractor program of the DESI Legacy Survey are reviewed by the public, who answer a set of identification questions. Using this model, they categorized 8.7 million objects from the DESI Legacy Survey (with a probabilistic label categorisation). From this catalog, we identified a total of 17,113 galaxies within a 45-arcminute radius from the 391 MALS pointing centers.

Initially, 109 galaxies with the highest vote fractions for the "Is this galaxy a merging-merger?" label were selected. From these, 13 merger-source pairs were identified where the radio contours overlapped with the visible images of the mergers. The radio data for the background sources were obtained from MALS. However, despite the promising appearance of the mergers in the visible images, none of the 13 background sources had a flux density high enough to exhibit any appreciable absorption signature.

Following this, we identified 39 galaxy-source pairs, this time without specifying any particular morphological classification for the galaxies. These searches were essentially conducted within the larger pool of 17,113 galaxies. Of the 39 pairs, 9 galaxies had redshift data available on NED. One of these merger-source pairs was contaminated by RFI, leaving us with 8 pairs for further analysis. The spectral data for these 8 sources were obtained using ARTIP [8]. Unfortunately, no HI absorption signatures were detected around the redshifted HI frequency of the galaxies in the source spectra. As a result, we calculated non-detection upper limits for these 8 pairs.

CHAPTER 5

BLIND SEARCH

In this chapter, we explore a unique approach to identifying HI absorption signatures by focusing solely on the spectral data of radio sources, without prior knowledge of the galaxies or intervening gas clouds. This method allows us to uncover the intervening and associated systems of HI absorption without bias, as we do not select objects based on their optical or morphological characteristics.

The primary aim of this technique is to detect signatures of neutral hydrogen (HI) that may indicate the presence of cold gas within the interstellar medium (ISM) along the line of sight of a strong radio source. By examining the spectra directly, we can potentially reveal interactions between galaxies and the gas in their vicinity, thereby gaining insights into star formation processes and the evolution of the ISM over cosmic time.

Among the sources analyzed, one particularly notable case is J135609 (or, NGC5363). This galaxy was identified through a compilation of sources provided by the MALS collaboration.[14] The spectra for NGC5363 were obtained using ARTIP.[8]

The spectral analysis of NGC5363 showed promising signs of absorption, suggesting the presence of HI along the line of sight. To further substantiate these findings, we conducted calculations based on the observed spectra and performed a literature survey to assess previous studies related to this source.

The results of this investigation highlights the potential of the blind search technique. In the following sections, we will detail the methodology applied to analyze the spectra of NGC5363, the calculations performed, and the relevant findings from the literature that support our observations.

5.1. Analysis of NGC5363

A total of 343 sources with their RA and DEC information for the peak pixel and peak flux values were obtained. These radio sources could either be part of an associated system where the absorption occurs within the accretion disk of an active galactic nucleus (AGN), or they could be intervening systems where a neutral hydrogen (HI) cloud along the line of sight imprints an absorption signature in the source's spectrum. The corresponding properties of the objects associated with the sources were identified using the catalogue that was built by extending the Galaxy Zoo categorisation of 8M objects in DESI Lecagy Survey DR8 using a machine learning model. [16]

The NED database was queried to find the corresponding redshift values for both the source and object coordinates within a 2-arcsecond radius. If the redshift of the source and the object were found to be identical, the system was classified as an associated AGN system. Conversely, if the redshifts differed, the system was classified as an intervening HI cloud.

Out of the 343 sources, redshift data was successfully obtained for 39 radio sources and 42 galaxy objects. Among these, only 11 systems had redshift data available for both the source-galaxy pairs. Redshift distributions of the selection is presented in Appendix C. Details about the 11 sources is presented in table 5.1.

Source Name	Peak Flux (mJy)	RA_S (hms)	DEC_S (dms)	Dist S-OBJ	OBJ ID	RA_OBJ (deg)	DEC_OBJ (deg)	Vote Frac	z_S	z_OBJ
J015454.30-000723.3	253.75161298976585	01:54:54.370	-00:07:23.800	3.283460274560787	$329042_{5}847$	28.690991	-0.164882	0.02	1.829241	0.079691
J052409.40-262015.9	389.719637379525	05:24:09.432	-26:20:17.041	0.0213975160554144	$184593_{1}276$	81.039413	-26.337725	0.03	0.29	0.29
J083601.29+040636.0	430.33279894592346	08:36:01.350	+04:06:36.000	1.3692303826285863	$353917_{4}540$	129.014846	4.089115	0.04	0.743	0.064354
J095428.68+130334.5	15.855000623586731	09:54:28.711	+13:03:34.578	0.0130925174295922	$405267_{2}915$	148.619843	13.05954	0.02	0.150205	0.150205
J122355.48+043104.2	8.795694112854479	12:23:55.546	+04:31:04.959	3.290383573610275	$357019_{1}464$	185.982151	4.463209	0.01	6.609112	0.212666
J123420.28+081152.3	10.148305530867813	12:34:20.257	+08:11:51.390	3.596746891220157	$378512_{1}104$	188.53148	8.168466	0.02	0.006551	0.102217
J123856.06-005930.1	16.827616679176053	12:38:56.048	-00:59:30.006	2.9604969709012616	$325366_{1}357$	189.732767	-1.041004	0.04	1.845218	0.0812
J135609.11+051503.9	164.18296707523226	13:56:07.226	+05:15:17.072	0.0124059550336041	$361419_{1}887$	209.030063	5.254944	0.05	0.003799	0.003799
J162303.00+123957.8	505.1990798448849	16:23:03.030	+12:39:58.400	2.0163905261102912	$404241_{1}816$	245.768508	12.699335	0.02	0.0	0.128265
J234022.58-115734.4	15.459976640499182	23:40:22.698	-11:57:35.328	0.0207265027814109	$263100_{3}109$	355.094866	-11.960009	0.03	0.185183	0.185183
J231632.49-431316.0	40.398018948594064	23:16:32.527	-43:13:16.751	1.7142125973879914	$105094_{3}319$	349.111803	-43.244067	0.02	0.005365	0.054418

Table 5.1.: Selection of 11 source-object pairs with their redshifts found from blind search.

An additional parameter for proximity was introduced to ensure that the galaxy object could have an appreciable absorption signature in the source's spectrum. Among the 11 pairs, only one pair fell within a 50 kpc limit for the angular diameter distance [22] between the central coordinates of the source and the galaxy in the galaxy plane. The 50 kpc threshold was chosen as it represents the typical diameter of a spiral galaxy. When this limit was extended to 500 kpc, a total of 4 source-object pairs were identified. All 4 of these pairs were associated systems, as the redshifts of the sources and objects were found to be equal. (Refer to the corresponding image cutouts (Fig [5.1]) of the 4 pairs.)

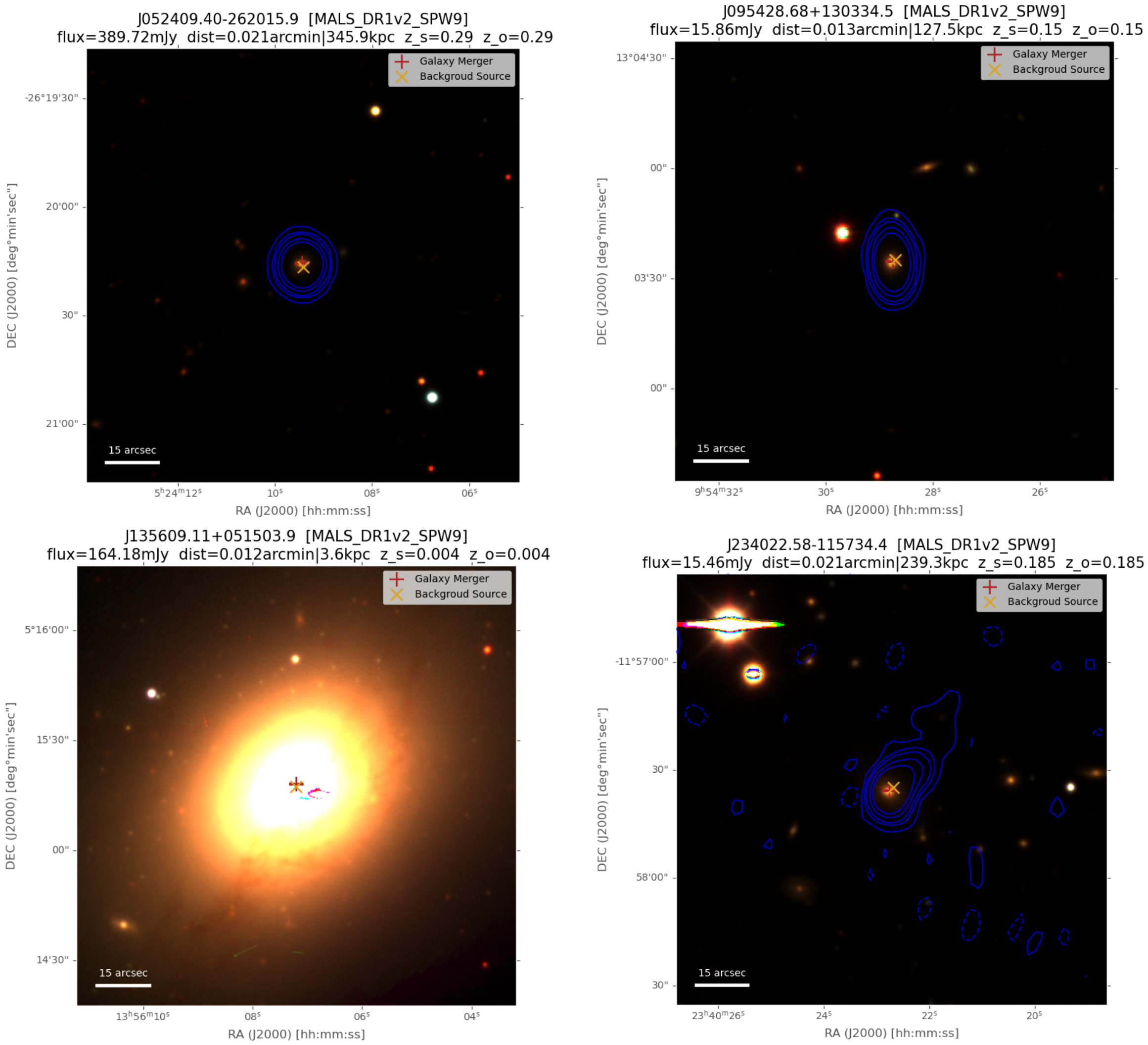

Figure 5.1.: Visible image cutouts with radio overlays for the 4 source-object pairs

For further analysis, the source within the 50 kpc limit, **J135609** associated with **NGC 5363** (also **UGC 8847**), was chosen. The redshift from NED database was $z_{NED} = 0.003799$.

The flux data for the source was processed using boxcar smoothing over five spectral windows. Fig [5.2]

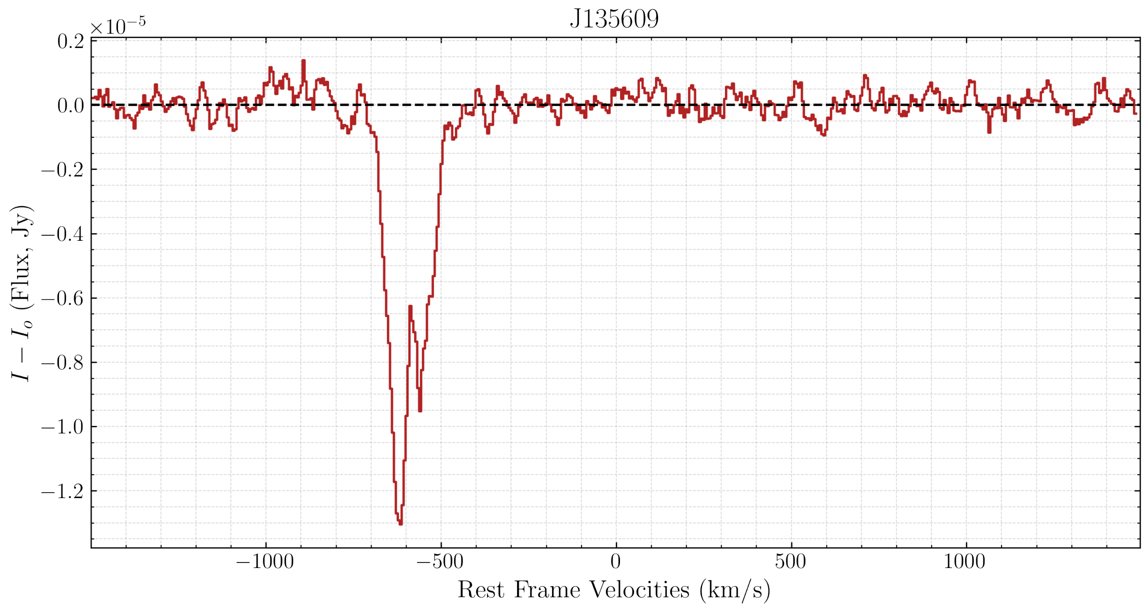

Figure 5.2.: Spectrum after smoothing

In our analysis, we considered the speed of light, $c = 299792.458\,\mathrm{km/s}$, and the rest frequency of neutral hydrogen, $\nu_{rest}^{HI} = 1420.405752\,\mathrm{MHz}$. The rest frame velocities from the data were converted to heliocentric frequencies using the following identity:

$$\nu_{obs} = \frac{\nu_{obs}^{HI}}{c} \times v_{rest} + \nu_{obs}^{HI}$$

where $\nu_{obs}^{HI} = \frac{\nu_{rest}^{HI}}{1+z_{NED}}$. The heliocentric frequencies were then converted to corrected rest frame velocities where the zero of velocity frame lies on the centroid of a single gaussian component fitted to the absorption signature observed. This was done using the following identity:

$$v_{rest} = \frac{c}{\nu_{obs}^{HI}} \left(\nu_{obs} - \nu_{obs}^{HI}\right)$$

where this time $\nu_{obs}^{HI} = \frac{\nu_{rest}^{HI}}{1+z_{MALS}}$. The new rest frame velocity are presented in the Fig [5.3]

A four-component gauss function was fitted to the flux at absorption signature which had a $\chi^2_{red} = 0.24$, Fig [5.4].

Following this, $v \in [-405.7, 594.6]$ were considered to calculate the optical depth (τ) values. Spin temperature (T_s) of $100K$ and a FWHM of $120 km/s$ was assumed for further analysis. The optical depth values calculated using the normalised flux. [10] [23]

$$\tau_i = -log\left(1 - \frac{I_i}{\sum I_i}\right)$$

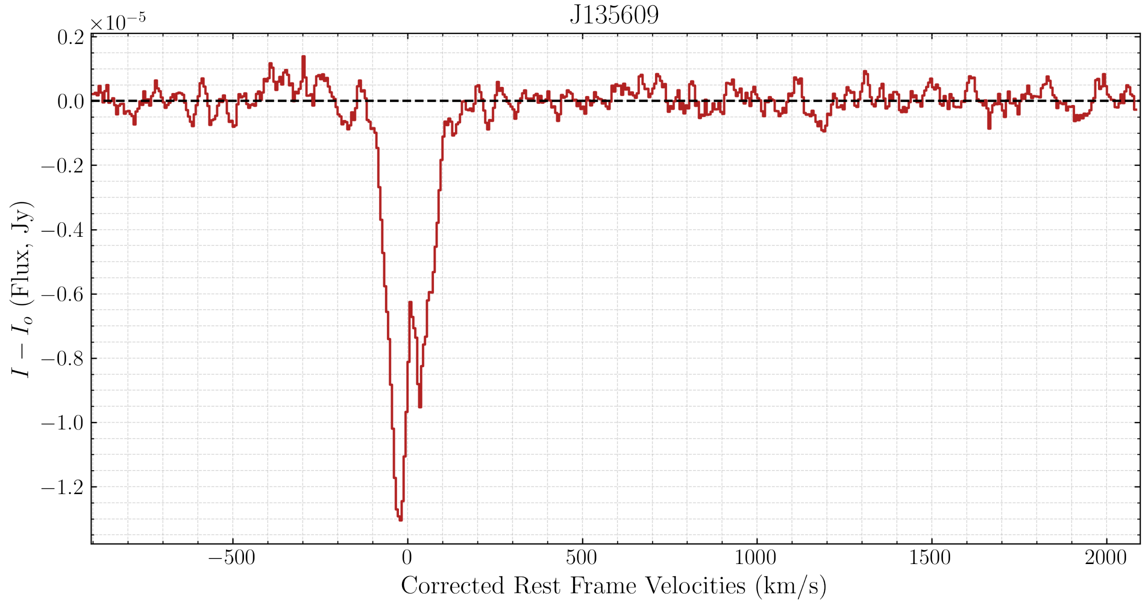

Figure 5.3.: Corrected Velocity Plots

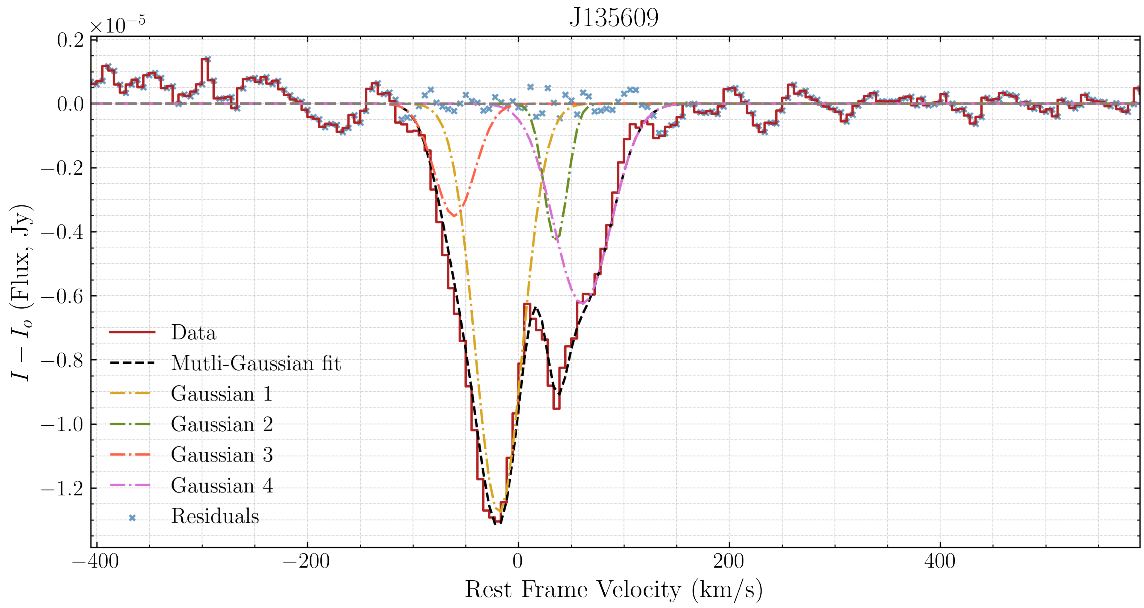

Figure 5.4.: 4-Component Gauss Fit to Flux

Integrated optical depth ($\int \tau \delta v$) was calculated by summing over the τ values and velocity width of $\Delta v = 5.55 km/s$. [10] [23]

$$\int \tau \delta v = \sum \tau_i \Delta v$$

Column density was calculated by (equation 1.7),

$$N(HI) = 1.823 \times 10^{18} T_s \int \tau \delta v$$

The errors for this observation was calculated by taking a median of all the errors values of flux as I_{rms} and [24],

$$\tau_{rms} = \frac{I_{rms}}{\sum I_i}$$

$$\left[\int \tau \delta v\right]_{err} = \tau_{rms} \times \delta v \times \left(\frac{2.54 \times FWHM}{\delta v}\right)^{-1/2}$$

$$[N(HI)]_{err} = 1.823 \times 10^{18} \times T_s \times \left[\int \tau \delta v\right]_{err}$$

A similar four-component gauss function was fitted to the optical depth values, and the $\int \tau dv = 5.7 \pm 0.1$ km/s and $N(HI) = 1.03 \pm 0.02 \times 10^{21} cm^{-2}$ were calculated with $\delta v = 5.5576$ km/s for a fit of $\chi^2 = 40.24$ and $\chi^2_{red} = 0.24$. (Fig [5.5])

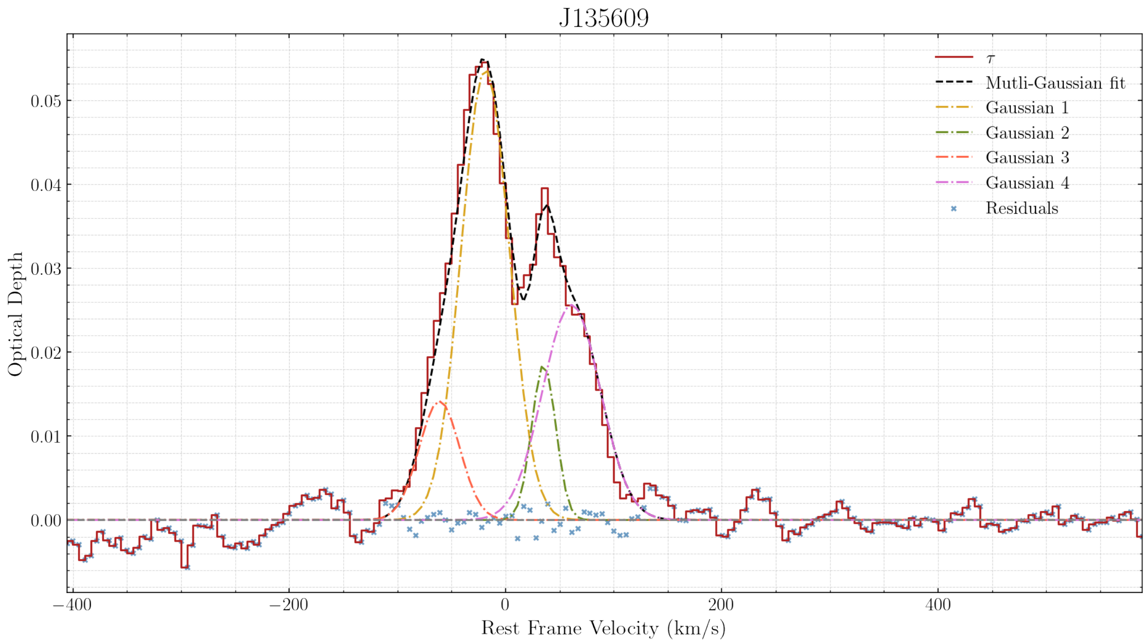

Figure 5.5.: 4-Component Gauss Fit to τ

5.2. Literature survey of NGC5363

NGC 5363 is a well-studied galaxy, frequently mentioned in surveys focused on active galactic nuclei (AGN) and radio cores. The most accurate redshift estimate for this galaxy is $z = 0.003799 \pm 0.000017$, as obtained from the Third Reference Catalogue of Bright Galaxies [25].

X-ray observations have revealed that dense neutral gas is present near the core of the radio source. NGC 5363 features X-ray absorption as cataloged in 3XMM-DR4 [26]. Moss et al. [27] found a significant correlation between the optical depth of HI absorption in the radio spectrum and the X-ray hardness ratio, suggesting that HI absorbers have lower energy levels in the soft X-ray region. [28]

Mid-infrared (MIR) observations of NGC 5363, a galaxy classified as Hubble type S0, show that dust in the interstellar medium (ISM) is concentrated near the center. Studies conducted with the ISOCAM instrument on the ISO satellite [29] observed dust emissions that provide insight into ionized gases and photo-dissociation regions. The dust temperature is estimated to be greater than $30\,K$, and the dust mass exceeds $6.9 \times 10^5\, M_{\odot}$.

CO emission has been used to trace star formation in NGC 5363, with the ratio of far-infrared (FIR) luminosity to H_2 mass suggesting a star formation rate comparable to that of the Milky Way [30]. The correlation between non-thermal radio flux and thermal FIR flux indicates that the formation of massive stars is independent of the global star formation rate. [31]

Despite being observed with GMRT and the Arecibo telescope, OH absorption signatures were not detected in NGC 5363 [32]. However, the galaxy's HI column density was measured to be $10.3 \times 10^{20}\,\mathrm{cm}^{-2}$, with a velocity shift of $+96\,\mathrm{km/s}$ relative to the optical emission lines. This galaxy is classified as a compact steep-spectrum (CSS) source.

Finally, parsec-scale jets have been observed in NGC 5363 [33], with multi-frequency VLBI data used to study the orientation of these jets. The visibility data were fitted with Gaussian models, enabling the determination of the jet angle relative to the core, with comparisons made to the MOJAVE program.

5.3. Conclusion

In this chapter, we demonstrated the "blind search" approach to identifying HI absorption signatures in radio source spectra. Unlike conventional methods, where one first searches for intervening gas clouds along the line of sight of a radio source with a potential absorption signature, the blind search method bypasses this step. Instead, we directly examine the radio spectra from MALS for any HI absorption features. A list of potential candidates for this study was provided by collaborators from the MALS project [14], and galaxy pairs with probabilistic morphological identification were cross-referenced using the catalog from [16].

From an initial list of 343 promising candidates, 11 systems were identified that had available redshift data for both the galaxy and the source on NED. Radio overlay images showed that, out of these 11, 4 systems exhibited radio contour overlaps with the visible images. All 4 galaxy-source pairs fell within a 500 kpc angular distance limit. Notably, for these 4 systems, the redshift data for both the galaxy and the source were approximately similar, indicating that they may represent associated systems with HI absorption.

Of these 4, one particularly interesting system was source J135609, associated with galaxy NGC5363, which was located within 50 kpc angular distance between the source and the galaxy. The spectra for this system, obtained via ARTIP [8], revealed a clear HI absorption signature. The column density values derived from this analysis were consistent with those reported in other published literature.

This analysis highlights the effectiveness of the blind search method, which successfully identified a significant HI absorption system. This approach shows great potential and will be further expanded in future studies to identify more absorption systems.

CHAPTER 6

SUMMARY & CONCLUSION

The detection of neutral hydrogen (HI) via its 21-cm absorption line remains one of the most powerful tools for studying the interstellar medium (ISM) and probing the cold gas content of galaxies. The HI 21-cm line allows us to trace gas that is crucial for star formation, revealing the fuel reservoirs that drive the evolutionary processes in galaxies. The ability to detect this gas at different redshifts also provides critical insights into galaxy evolution over cosmic time, enabling us to understand how galaxies accumulate and exhaust their gas supplies.

6.1. Short Summary of Work

In the study of HI absorption, two principal approaches can be adopted. The first involves targeting specific galaxies or known objects of interest, where we directly investigate the presence of neutral hydrogen based on previously established properties of the galaxies. This method is highly focused, typically yielding information about the ISM properties of specific galaxies or interactions.

The second approach involves conducting a "blind search" for HI absorption. In this method, instead of targeting known galaxies or objects of interest, we examine radio spectra without preconceived selection criteria. This allows for the unbiased discovery of HI absorption signatures, providing a powerful method for identifying intervening and associated systems that may not be immediately apparent from optical surveys. The blind search method is advantageous as it offers a broader view of how cold gas may be distributed throughout the universe, not just in known galaxies.

In the course of this project, we identified multiple cases of HI absorption signatures through a blind search. However, this thesis presents one such source in detail: NGC 5363, whose spectrum showed promising absorption features. The analysis of this system, including the calculations and a thorough literary review, underscores the potential of blind searches to uncover significant cold gas reservoirs that might otherwise be missed in galaxy-targeted studies.

6.2. Conclusion

The research presented in this thesis addresses a highly relevant topic in the broader field of radio astronomy: the study of star formation rates (SFR) and the survey of cold gases in and around galaxies, particularly at redshifts $z < 0.6$. Understanding the distribution and behavior of these cold gases is crucial, as they play a key role in the formation and evolution of galaxies. This redshift range has been identified as a priority for advancing our understanding of galaxy evolution, and studies like this are essential for filling existing gaps in knowledge.

The research leveraged one of the most powerful and sensitive radio telescopes available today—MeerKAT, a precursor to the Square Kilometre Array (SKA). MeerKAT's excellent sensitivity and resolution make it ideal for detecting faint absorption signatures from cold gas, even at relatively high redshifts. This thesis is based on the MeerKAT Absorption Line Survey (MALS), which is one of the most promising and ambitious projects in the field of radio astronomy, aiming to catalog HI and OH absorption lines over a wide redshift range.

While our initial approach, which involved identifying promising galaxy morphologies before checking their spectra, did not yield the desired results, this study demonstrates the importance of employing different search strategies. By exploring both targeted and blind search methods for absorption signatures, we were able to understand the strengths and limitations of each. This led to the conclusion that the first method, while theoretically sound, was not feasible in practice for the dataset we were working with.

In contrast, the blind search approach proved to be more effective. The promising candidate we identified and analyzed serves as a proof of concept for the blind search method. Though only one source was presented in detail here, this analysis paves the way for future work. The methodology will be extended to more candidate sources, allowing for a more comprehensive understanding of cold gas absorption in galaxies. The results from this work will be instrumental for any future publications, contributing valuable insights to the broader scientific community.

The findings of this thesis not only advance our knowledge of cold gas in the universe but also contributes to future investigations that will utilize the data from MALS and other radio surveys. The ongoing analysis of additional sources and the potential for further discoveries demonstrate the potential impact of this research on the field of extragalactic radio astronomy.

6.3. Future Prospects

Looking ahead, the next phase of this research will involve expanding the scope of the blind search to statistically interpret the distribution of cold gas in the ISM across a larger sample of spectra. By analyzing the complete set of spectra in the MeerKAT Absorption Line Survey (MALS) datasets, we aim to gain a deeper understanding of how cold gas is spread across different environments. This broader statistical interpretation will provide key insights into the star formation history of our universe. Ultimately, this work contributes to the future investigations into the role of cold gas in galaxy evolution, leveraging the power of blind HI absorption searches to open new frontiers in our understanding of the universe.

APPENDIX A

Section 1.2

Phase	$T(\mathrm{K})$	$n_{\mathrm{H}}(\mathrm{cm}^{-3})$	Comments
Coronal gas (HIM) $f_V \approx 0.5?$ $\langle n_{\mathrm{H}} \rangle f_V \approx 0.002\,\mathrm{cm}^{-3}$ ($f_V \equiv$ volume filling factor)	$\gtrsim 10^{5.5}$	~ 0.004	Shock-heated Collisionally ionized Either expanding or in pressure equilibrium Cooling by: ◇ Adiabatic expansion ◇ X ray emission Observed by: • UV and x ray emission • Radio synchrotron emission
H II gas $f_V \approx 0.1$ $\langle n_{\mathrm{H}} \rangle f_V \approx 0.02\,\mathrm{cm}^{-3}$	10^4	$0.3 - 10^4$	Heating by photoelectrons from H, He Photoionized Either expanding or in pressure equilibrium Cooling by: ◇ Optical line emission ◇ Free–free emission ◇ Fine-structure line emission Observed by: • Optical line emission • Thermal radio continuum
Warm H I (WNM) $f_V \approx 0.4$ $n_{\mathrm{H}} f_V \approx 0.2\,\mathrm{cm}^{-3}$	$\sim$5000	0.6	Heating by photoelectrons from dust Ionization by starlight, cosmic rays Pressure equilibrium Cooling by: ◇ Optical line emission ◇ Fine structure line emission Observed by: • H I 21 cm emission, absorption • Optical, UV absorption lines
Cool H I (CNM) $f_V \approx 0.01$ $n_{\mathrm{H}} f_V \approx 0.3\,\mathrm{cm}^{-3}$	~ 100	30	Heating by photoelectrons from dust Ionization by starlight, cosmic rays Cooling by: ◇ Fine structure line emission Observed by: • H I 21-cm emission, absorption • Optical, UV absorption lines
Diffuse H_2 $f_V \approx 0.001$ $n_{\mathrm{H}} f_V \approx 0.1\,\mathrm{cm}^{-3}$	$\sim 50\,\mathrm{K}$	~ 100	Heating by photoelectrons from dust Ionization by starlight, cosmic rays Cooling by: ◇ Fine structure line emission Observed by: • H I 21-cm emission, absorption • CO 2.6-mm emission • optical, UV absorption lines
Dense H_2 $f_V \approx 10^{-4}$ $\langle n_{\mathrm{H}} \rangle f_V \approx 0.2\,\mathrm{cm}^{-3}$	$10 - 50$	$10^3 - 10^6$	Heating by photoelectrons from dust Ionization and heating by cosmic rays Self-gravitating: $p > p$(ambient ISM) Cooling by: ◇ CO line emission ◇ C I fine structure line emission Observed by: • CO 2.6-mm emission • dust FIR emission
Cool stellar outflows	$50 - 10^3$	$1 - 10^6$	Observed by: • Optical, UV absorption lines • Dust IR emission • H I, CO, OH radio emission

Figure A.1.: Different Phases of Interstellar Gas [2]

APPENDIX B

Section 4.4

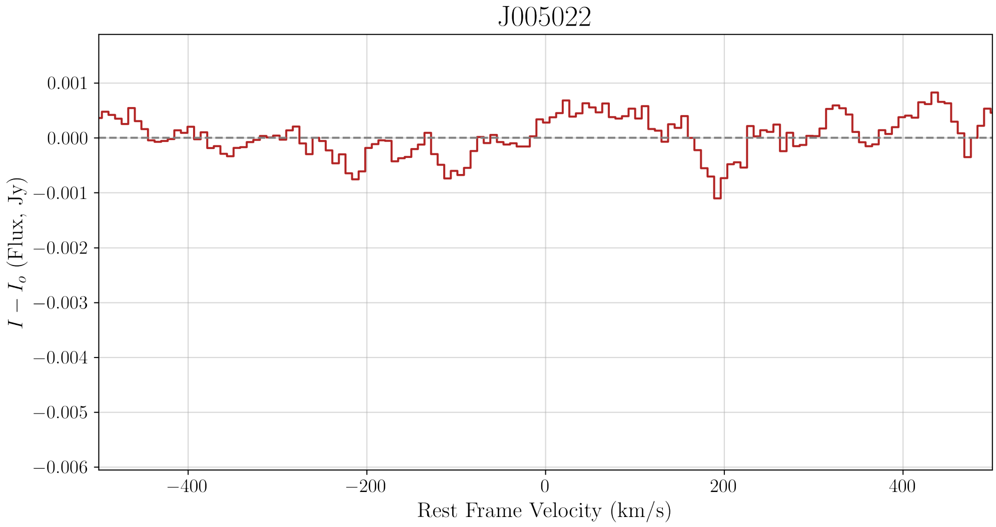

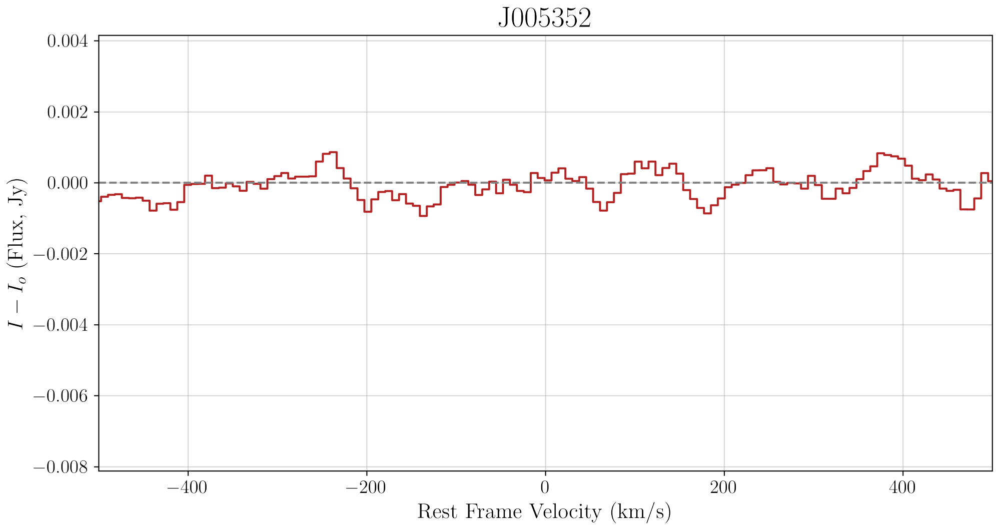
J005352
0.004
0.002
0.000
−0.002
−0.004
−0.006
−0.008
$I - I_o$ (Flux, Jy)
−400
−200
0
200
400
Rest Frame Velocity (km/s)

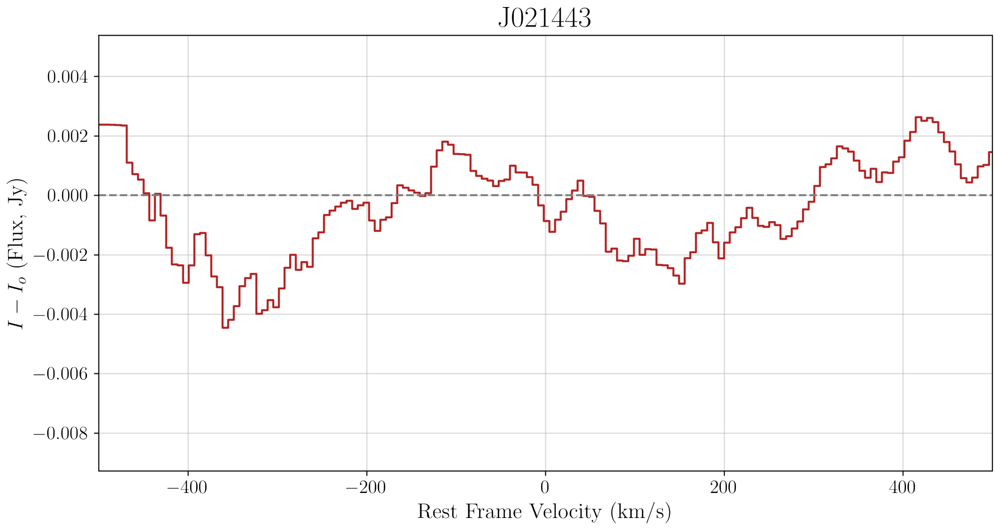
J021443
0.004
0.002
0.000
−0.002
−0.004
−0.006
−0.008
$I - I_o$ (Flux, Jy)
−400
−200
0
200
400
Rest Frame Velocity (km/s)

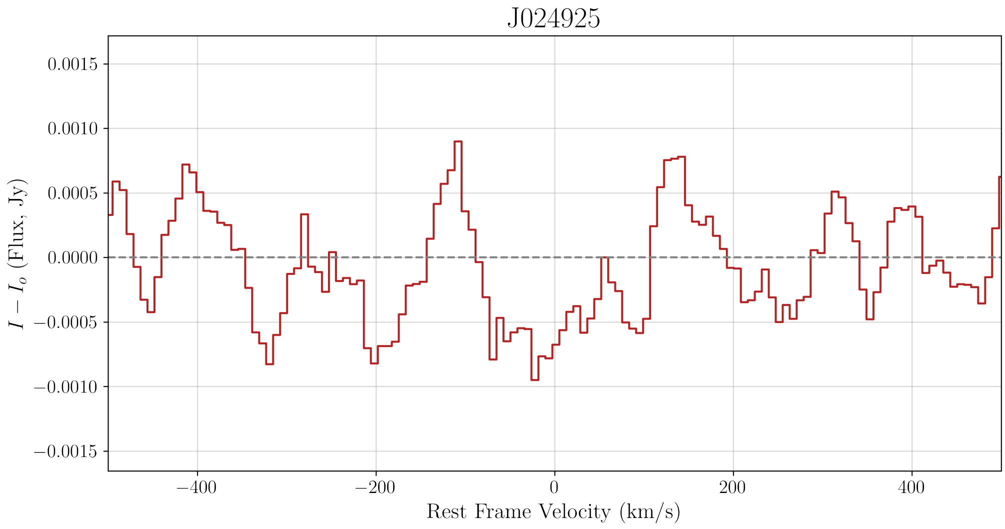
J024925
0.0015
0.0010
0.0005
0.0000
−0.0005
−0.0010
−0.0015
$I - I_o$ (Flux, Jy)
−400
−200
0
200
400
Rest Frame Velocity (km/s)

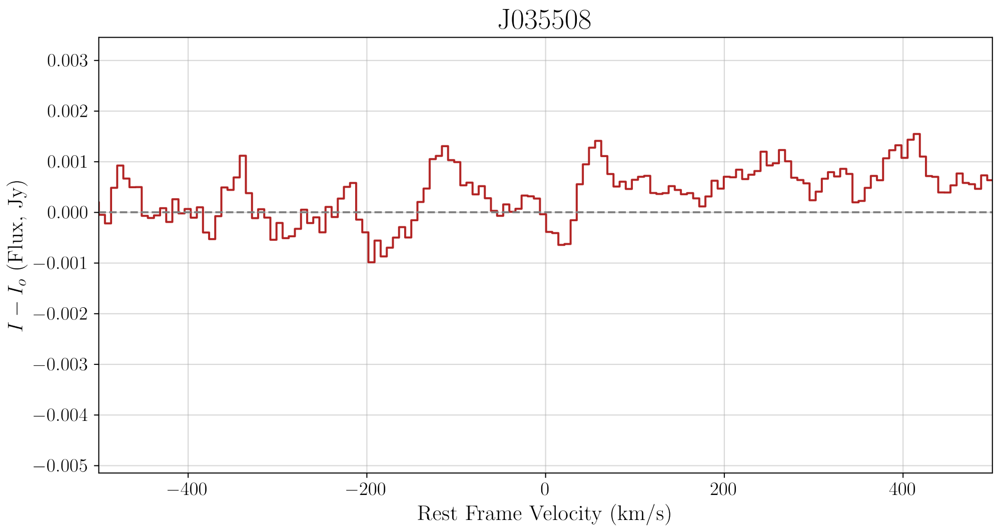
J035508
0.003
0.002
0.001
0.000
−0.001
−0.002
−0.003
−0.004
−0.005
$I - I_o$ (Flux, Jy)
−400
−200
0
200
400
Rest Frame Velocity (km/s)

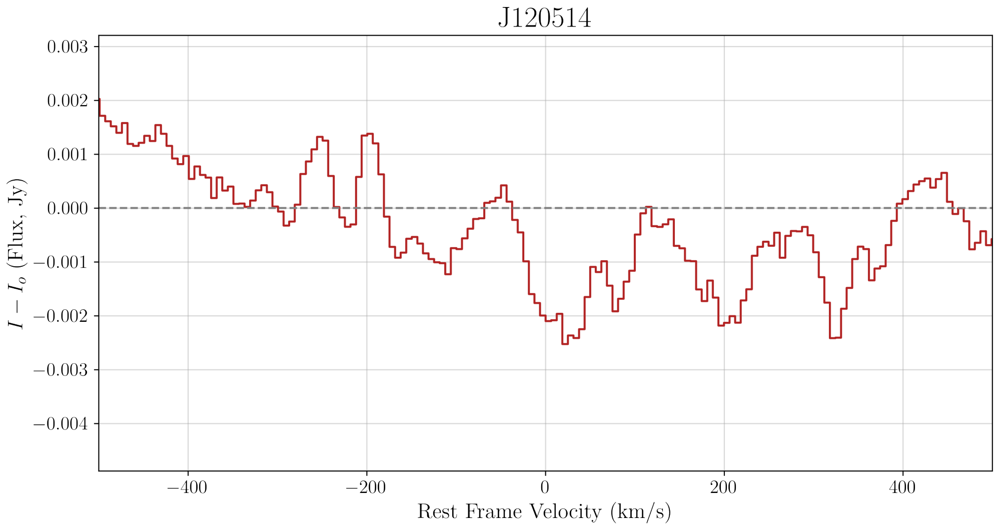
J120514
0.003
0.002
0.001
0.000
−0.001
−0.002
−0.003
−0.004
$I - I_o$ (Flux, Jy)
−400
−200
0
200
400
Rest Frame Velocity (km/s)

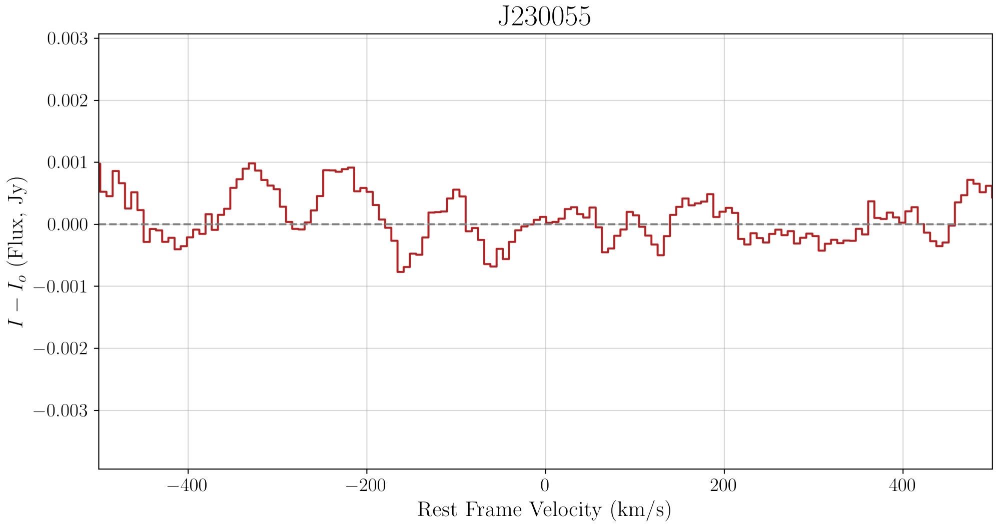
J230055
0.003
0.002
0.001
0.000
−0.001
−0.002
−0.003
$I - I_o$ (Flux, Jy)
−400
−200
0
200
400
Rest Frame Velocity (km/s)

APPENDIX C

Section 5.1

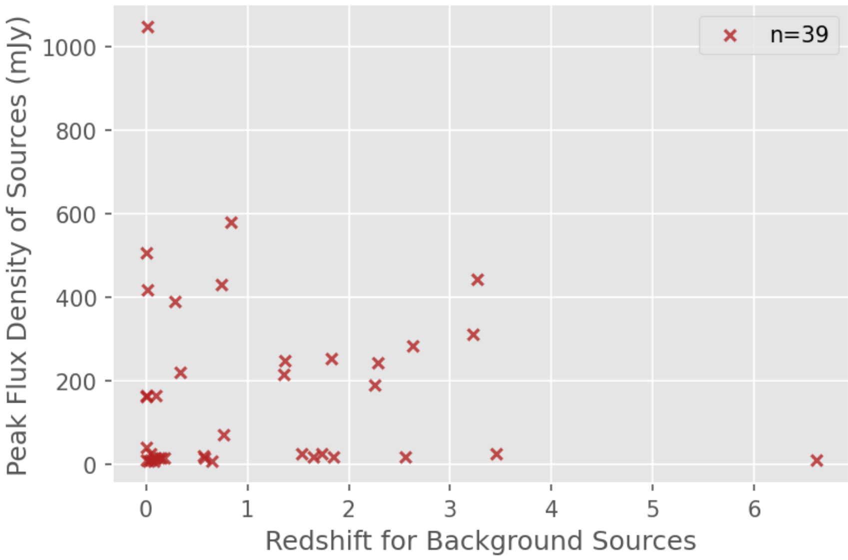

Figure C.1.: Flux vs. z_s

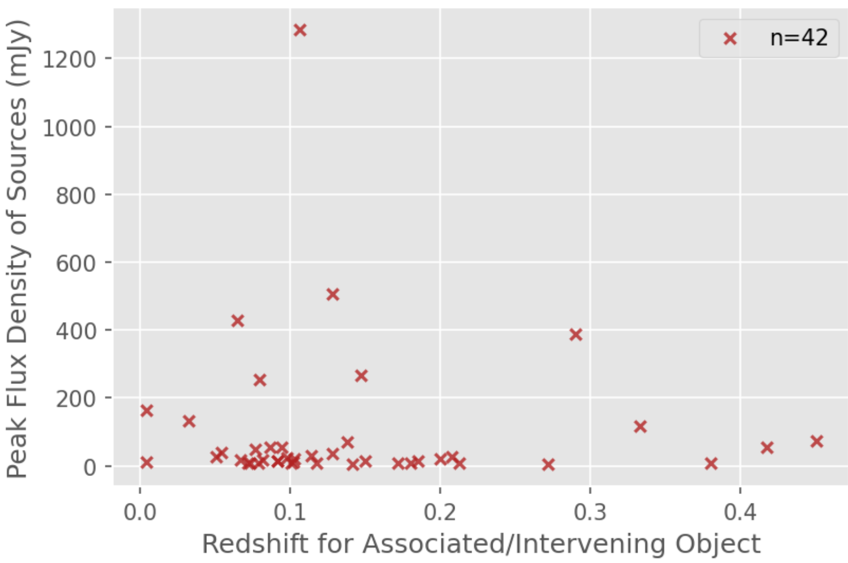

Figure C.2.: Flux vs. z_g

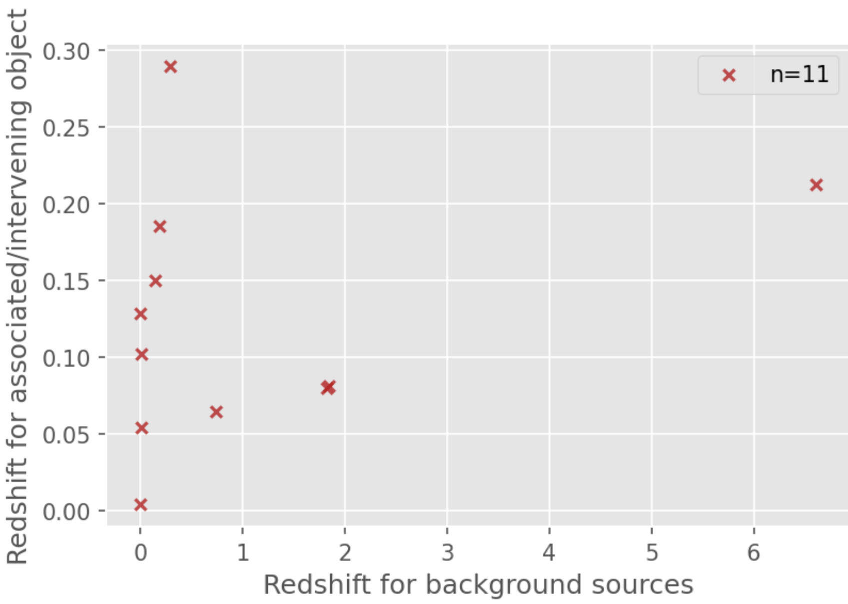

Figure C.3.: z_g vs. z_s

Bibliography

[1] I. Zehavi, Z. Zheng, D. H. Weinberg, M. R. Blanton, N. A. Bahcall, A. A. Berlind, J. Brinkmann, J. A. Frieman, J. E. Gunn, R. H. Lupton *et al.*, "Galaxy clustering in the completed sdss redshift survey: the dependence on color and luminosity," *The Astrophysical Journal*, vol. 736, no. 1, p. 59, 2011.

[2] B. T. Draine, *Physics of the interstellar and intergalactic medium.* Princeton University Press, 2010, vol. 19.

[3] P. M. Kalberla, W. Burton, D. Hartmann, E. M. Arnal, E. Bajaja, R. Morras, and W. G. Pöppel, "The leiden/argentine/bonn (lab) survey of galactic hi-final data release of the combined lds and iar surveys with improved stray-radiation corrections," *Astronomy & Astrophysics*, vol. 440, no. 2, pp. 775–782, 2005.

[4] J. J. Condon and S. M. Ransom, *Essential radio astronomy.* Princeton University Press, 2016, vol. 2.

[5] B. F. Burke, F. Graham-Smith, and P. N. Wilkinson, *An introduction to radio astronomy.* Cambridge University Press, 2019.

[6] NRAO, "Vla casa imaging-casa5.0.0," https://casaguides.nrao.edu/index.php/VLA_CASA_Imaging-CASA5.0.0, [Accessed 26-04-2024].

[7] B. Bean, S. Bhatnagar, S. Castro, J. D. Meyer, B. Emonts, E. Garcia, R. Garwood, K. Golap, J. G. Villalba, P. Harris *et al.*, "Casa, the common astronomy software applications for radio astronomy," *Publications of the Astronomical Society of the Pacific*, vol. 134, no. 1041, p. 114501, 2022.

[8] N. Gupta, P. Jagannathan, R. Srianand, S. Bhatnagar, P. Noterdaeme, F. Combes, P. Petitjean, J. Jose, S. Pandey, C. Kaski *et al.*, “Blind h i and oh absorption line search: first results with mals and ugmrt processed using artip,” *The Astrophysical Journal*, vol. 907, no. 1, p. 11, 2021.

[9] K. Rohlfs and T. L. Wilson, *Tools of radio astronomy.* Springer Science & Business Media, 2013.

[10] E. Maina, A. Mohapatra, G. Józsa, N. Gupta, F. Combes, P. Deka, J. Wagenveld, R. Srianand, S. Balashev, H.-W. Chen *et al.*, “Mapping h i 21-cm in the klemola 31 group at z= 0.029: emission and absorption towards pks 2020- 370,” *Monthly Notices of the Royal Astronomical Society*, vol. 516, no. 2, pp. 2050–2061, 2022.

[11] N. Kanekar and F. Briggs, “21-cm absorption studies with the square kilometer array,” *New Astronomy Reviews*, vol. 48, no. 11-12, pp. 1259–1270, 2004.

[12] T. Westmeier, R. Jurek, D. Obreschkow, B. S. Koribalski, and L. Staveley-Smith, “The busy function: a new analytic function for describing the integrated 21-cm spectral profile of galaxies,” *Monthly Notices of the Royal Astronomical Society*, vol. 438, no. 2, pp. 1176–1190, 2014.

[13] P. C. Clark and S. C. Glover, “On column density thresholds and the star formation rate,” *Monthly Notices of the Royal Astronomical Society*, vol. 444, no. 3, pp. 2396–2414, 2014.

[14] N. Gupta, R. Srianand, W. Baan, A. Baker, R. Beswick, S. Bhatnagar, D. Bhattacharya, A. Bosma, C. Carilli, M. Cluver *et al.*, “The meerkat absorption line survey (mals),” *arXiv preprint arXiv:1708.07371*, 2017.

[15] A. R. Thompson, J. M. Moran, and G. W. Swenson, *Interferometry and synthesis in radio astronomy.* Springer Nature, 2017.

[16] M. Walmsley, T. Géron, S. Kruk, A. M. Scaife, C. Lintott, K. L. Masters, J. M. Dawson, H. Dickinson, L. Fortson, I. L. Garland *et al.*, “Galaxy zoo desi: Detailed morphology measurements for 8.7 m galaxies in the desi legacy imaging surveys,” *Monthly Notices of the Royal Astronomical Society*, vol. 526, no. 3, pp. 4768–4786, 2023.

[17] K. Grainge, B. Alachkar, S. Amy, D. Barbosa, M. Bommineni, P. Boven, R. Braddock, J. Davis, P. Diwakar, V. Francis *et al.*, “Square kilometre array: The radio telescope of the xxi century,” *Astronomy reports*, vol. 61, pp. 288–296, 2017.

[18] P. Deka, N. Gupta, P. Jagannathan, S. Sekhar, E. Momjian, S. Bhatnagar, J. Wagenveld, H.-R. Klöckner, J. Jose, S. Balashev *et al.*, "The meerkat absorption line survey (mals) data release. i. stokes i image catalogs at 1–1.4 ghz," *The Astrophysical Journal Supplement Series*, vol. 270, no. 2, p. 33, 2024.

[19] R. Dutta, R. Srianand, and N. Gupta, "Prevalence of neutral gas in centres of merging galaxies," *Monthly Notices of the Royal Astronomical Society*, vol. 480, no. 1, pp. 947–964, 2018.

[20] A. Dey, D. J. Schlegel, D. Lang, R. Blum, K. Burleigh, X. Fan, J. R. Findlay, D. Finkbeiner, D. Herrera, S. Juneau *et al.*, "Overview of the desi legacy imaging surveys," *The Astronomical Journal*, vol. 157, no. 5, p. 168, 2019.

[21] M. Meyer, A. Robotham, D. Obreschkow, T. Westmeier, A. R. Duffy, and L. Staveley-Smith, "Tracing hi beyond the local universe," *Publications of the Astronomical Society of Australia*, vol. 34, p. e052, 2017.

[22] D. W. Hogg, "Distance measures in cosmology," *arXiv preprint astro-ph/9905116*, 1999.

[23] N. Gupta, R. Srianand, P. Petitjean, P. Noterdaeme, and D. Saikia, "A complete sample of 21-cm absorbers at z 1.3: Giant metrewave radio telescope survey using mg ii systems," *Monthly Notices of the Royal Astronomical Society*, vol. 398, no. 1, pp. 201–220, 2009.

[24] Y. Chandola, D. Saikia, and D. Li, "H i absorption towards radio active galactic nuclei of different accretion modes," *Monthly Notices of the Royal Astronomical Society*, vol. 494, no. 4, pp. 5161–5177, 2020.

[25] G. De Vaucouleurs, A. de Vaucouleurs, G. Harold Jr, R. J. Buta, G. Paturel, P. Fouqué *et al.*, *Third Reference Catalogue of Bright Galaxies: Volume III.* Springer Science & Business Media, 2013, vol. 3.

[26] S. Rosen, N. Webb, M. Watson, J. Ballet, D. Barret, V. Braito, F. Carrera, M. Ceballos, M. Coriat, R. Della Ceca *et al.*, "The xmm-newton serendipitous survey-vii. the third xmm-newton serendipitous source catalogue," *Astronomy & Astrophysics*, vol. 590, p. A1, 2016.

[27] V. Moss, J. Allison, E. Sadler, R. Urquhart, R. Soria, J. Callingham, S. Curran, A. Musaeva, E. Mahony, M. Glowacki *et al.*, "Connecting x-ray absorption and 21 cm neutral hydrogen absorption in obscured radio agn," *Monthly Notices of the Royal Astronomical Society*, vol. 471, no. 3, pp. 2952–2973, 2017.

[28] J. Wilms, A. Allen, and R. McCray, "On the absorption of x-rays in the interstellar medium," *The Astrophysical Journal*, vol. 542, no. 2, p. 914, 2000.

[29] E. M. Xilouris, S. Madden, F. Galliano, L. Vigroux, and M. Sauvage, "Dust emission in early-type galaxies: The mid-infrared view," *Astronomy & Astrophysics*, vol. 416, no. 1, pp. 41–55, 2004.

[30] D. Sanders and I. Mirabel, "Co detections and iras observations of bright radio spiral galaxies at cz equal or less than 9000 kilometers per second," *Astrophysical Journal, Part 2-Letters to the Editor (ISSN 0004-637X), vol. 298, Nov. 15, 1985, p. L31-L35. Research supported by the Universidad de Puerto Rico and NASA.*, vol. 298, pp. L31–L35, 1985.

[31] D. Narayanan and M. R. Krumholz, "A theory for the excitation of co in star-forming galaxies," *Monthly Notices of the Royal Astronomical Society*, vol. 442, no. 2, pp. 1411–1428, 2014.

[32] N. Gupta, C. Salter, D. Saikia, T. Ghosh, and S. Jeyakumar, "Probing radio source environments via h i and oh absorption," *Monthly Notices of the Royal Astronomical Society*, vol. 373, no. 3, pp. 972–992, 2006.

[33] A. Plavin, Y. Kovalev, and A. Pushkarev, "Direction of parsec-scale jets for 9220 active galactic nuclei," *The Astrophysical Journal Supplement Series*, vol. 260, no. 1, p. 4, 2022.